AIAA JOURNAL
Vol. 53, No. 12, December 2015

Numerical Predictions of Turbulence/Cascade-Interaction Noise Using Computational Aeroacoustics with a Stochastic Model

C. Polacsek,* V. Clair,† T. Le Garrec,* and G. Reboul*
ONERA–The French Aerospace Lab., 92322 Châtillon, France
and
M. C. Jacob‡
Université Claude Bernard Lyon I, 69622 Villeurbanne Cedex, France

DOI: 10.2514/1.J053896

Turbulent-flow interactions with the outlet guide vanes are known to mainly contribute to broadband-noise emission of aeroengines at approach conditions. This paper presents a three-dimensional computational aeroacoustics hybrid method aiming at simulating the aeroacoustic response of an annular cascade impacted by a prescribed homogeneous isotropic turbulent flow. It is based on a time-domain Euler solver coupled to a synthetic turbulence model implemented in the code by means of a suited inflow boundary condition. The fluctuating pressure over the airfoil surface provided by computational aeroacoustics is used as an input to a Ffowcs Williams and Hawkings integral method to calculate the radiated sound field. Euler computations are first validated against an academic computational aeroacoustics benchmark in the case of an harmonic gust interacting with an annular flat-plate cascade. Then, simulations are applied to turbulence–cascade interactions for annular configurations, in uniform and swirling mean flows, and numerical results in terms of sound power spectra in the outlet duct are compared to semi-analytical and numerical solutions, and to an available experiment.

Nomenclature

B	=	blade number
c	=	chord
f	=	frequency
k	=	wave number
L	=	span
M, M_x, M_θ	=	total, axial, azimuthal mean-flow Mach number
m, m_g	=	acoustic spinning-mode order, gust spinning-mode order
p, p_∞	=	static pressure, undisturbed static pressure
T_u	=	turbulence intensity
U_0, U_x	=	uniform, axial mean-flow velocity
u'	=	velocity disturbance
V	=	vane number
(x, r, θ)	=	cylindrical coordinates in the annular duct
Δk, Δf	=	wave number and frequency spacing
Λ	=	integral length scale
(ξ, η, r)	=	local coordinates attached to the vane
ρ, ρ_∞	=	density, undisturbed density
$\phi(k_x, k_r)$	=	two-wave-number turbulent energy spectrum
φ	=	random phase
χ	=	stagger angle
ω	=	angular frequency

I. Introduction

TURBULENT wakes generated by turbofan blades and interacting with the outlet guide vanes are known to mainly contribute to the broadband-noise emission of aeroengines at approach conditions. Analytical approaches, such as Amiet's [1] isolated airfoil or Hanson's [2] cascade models, can be adopted to estimate the noise generated by turbulent flows impacting thin airfoils, but they are limited by the flat-plate assumptions. Despite some recent attempts [3–5], reliable rotor–stator turbulent-interaction sources are still out of reach of common computational fluid dynamics (CFD) solvers based on large-eddy simulation or detached-eddy-simulation approaches. These simulations are generally restricted to a radial strip and to a single vane channel by enforcing periodicity conditions, and it should be more considered for capturing the three-dimensional (3-D) turbulent wake behind an isolated rotor blade as investigated, for example, in [6]. Recently, the lattice Boltzmann method (LBM) has been firstly applied to turbomachinery-noise problems with an impressive direct acoustic simulation performed by Exa [7] on the NASA Glenn Research Center's Advanced Noise Control Fan model, including the full rotor–stator stage and the wind-tunnel walls. The LBM technique appears to be a quite promising way to face present limitations in terms of current CPU capabilities.

Another approach [8] based on a computational aeroacoustics (CAA)/Euler hybrid methodology coupled to a synthetic turbulence inflow can also be considered, as investigated by recent studies [9–11], and is the object of the present paper. Here, we suggest to numerically assess the aerodynamic response of annular grids impacted by a prescribed turbulent velocity field, instead of using airfoil or cascade flat-plate response models adopted in the semi-analytical prediction tools. The turbulent wake generation from the rotor blades, devoted to CFD, is discarded in the present study.

The method is described in the first part of the paper, focusing on the way of modeling and injecting a synthetic turbulent flow (in terms of solenoidal velocity disturbances) in a CAA Euler code developed at ONERA [12,13], respectively, using a prescribed isotropic homogeneous turbulence-kinetic-energy (TKE) spectrum expanded into spatial Fourier modes, and a suited boundary condition (BC) proposed by Tam [14].

In the second part, the numerical simulations are validated against an academic benchmark related to a 3-D annular cascade impacted by a swirling harmonic gust in a uniform axial mean flow proposed by Namba and Schulten [15]. The CAA results are compared to the

Presented as Paper 2014-2453 at the 20th AIAA/CEAS Aeroacoustics Conference, Atlanta, GA, 16–20 June 2014; received 3 September 2014; revision received 28 January 2015; accepted for publication 9 March 2015; published online 7 October 2015.

*Research Engineer, CFD and Aeroacoustics Department; cyril.polacsek@onera.fr.

†Ph.D.; currently Research Fellow, Institute of Sound and Vibration Research, University of Southampton, SO17 1BJ Southampton, United Kingdom; V.J.Clair@soton.ac.uk.

‡Assistant Professor, Laboratoire de Mécanique des Fluides et d'Acoustique, CNRS–UMR 5509; marc.jacob@ec-lyon.fr.

semi-analytical solutions addressed by Namba [16] and Schulten [17]. For this test case, the acoustic response of the cascade (in-duct sound field) is directly assessed by the CAA.

Then, the method is applied to the simulation of turbulence/cascade-interaction noise on two selected configurations: 1) a turbulence/annular-cascade interaction in a uniform axial mean flow, related to a laboratory experiment performed in the anechoic open-jet wind tunnel of École Centrale de Lyon (ECL) [18] and chosen as a fundamental case in the framework of a recent workshop on broadband-turbofan-noise prediction [19]; and 2) a turbulence/annular-cascade interaction in a swirling mean flow, related to a benchmark proposed by Atassi and Vinogradov [20], with a reference solution issued from the frequency-domain linearized Euler code developed by Atassi et al. [21].

For these more complex cases involving broadband sources, the CAA domain is limited to a single vane channel, and azimuthal dependency of synthetic turbulent inflow is discarded, which permits to use periodic BCs in the angular direction. With these restrictions, direct acoustic field cannot be provided anymore by the CAA. The sound radiation in the outlet duct is obtained by means of a Ffowcs Williams and Hawkings (FWH) formulation (restricted to the loading-noise term) generalized by Goldstein [22] for annular ducts, using the CAA pressure fluctuations along the vane surface as input data, and assuming a fully uniform flow in the propagation (even for the swirling mean-flow case). The present numerical predictions of in-duct power spectrum density (PSD) in the outlet duct (downstream of the cascade) are compared to available measurements and analytical solutions too, issued from the Amiet [1] theory extended to ducted fans [23,24] and advanced 3-D lifting-surface calculations [25]. The Amiet-based formulation developed by Reboul [24] with proper expressions used in the ONERA's updated code is addressed in the Appendix. Thus, challenging issues related to cascade and swirling mean-flow effects on sound radiation, as well as the reliability of the simplifications adopted in the present CAA when simulating the incoming turbulent flow, are both discussed.

II. Hybrid Method Based on Stochastic Model Coupled to CAA

The simulations are performed using the ONERA code sAbrinA.v0 [12,13] solving the nonlinearized Euler equation or linearized Euler equation (LEE) in the time domain with a perturbation form that consists in a splitting of the conservative variables into a mean flow and a disturbance field. The spatial derivatives are computed using a 6th-order finite difference scheme, and a 10th-order explicit filter is applied to remove high-frequency oscillations. This allows to avoid numerical dispersion and dissipation effects for grids satisfying at least a 10-points-per-wavelength condition. The time evolution is achieved using a 3rd-order Runge–Kutta scheme. To perform rotor–stator interaction problems through CAA linearized Euler calculations, efficient numerical BCs (asymptotic solutions of the LEE) derived by Tam [14] have been implemented in the code [8] to allow velocity perturbations to be imposed at the inflow boundary. Although Tam's BCs are initially written in two-dimensional (2-D) polar coordinates, a more suited form extended to spherical coordinates [26] is used for ducted cascade calculations. As done in [26], a sponge zone (overfiltering), combined to a mesh stretching, is applied too at the exit of the CAA domain to allow both hydrodynamic and acoustic outgoing waves to leave the domain without generating spurious numerical reflections. A literature review and an investigation of advanced synthetic turbulence-generation models devoted to turbofan applications have been recently studied by Sescu [27]. The proposed stochastic model is the simplest and is similar to Kraichnan's theory [28]. As proposed by Kraichnan and also adopted in [29], it is based on a Fourier-mode decomposition of the incoming turbulent wake modeled by a homogeneous-isotropic-turbulence (HIT) energy spectrum, but restricted here to the upwash-velocity component (normal to the airfoil assimilated to a flat plate) by analogy with Amiet's [1] theory. Such an approach aims to reproduce the statistical energy of the prescribed TKE spectrum in the frequency domain without trying to capture any space–time correlation scales, which is different to time-domain random-particle-mesh (RPM) methods extensively used by Ewert [30]. However, 2-D and 3-D turbulence–airfoil simulations studied in [8] were found to be as much accurate as those (only 2-D) reported in [9] using the RPM approach. Moreover, to limit the size of the CAA domain and CPU cost, and following the approach of Casper and Farassat [31], the synthetic turbulence is described here by a two-wave-number spectrum (3-D spectrum integrated over the azimuthal wave numbers), with a spatial distribution over the streamwise and spanwise directions. Thus, neglecting the azimuthal-wave-number dependency of the TKE spectrum, the two-wave-number-spectrum approach suggested by Clair et al. [8] for simulating a turbulence–airfoil problem is reconsidered here for the present annular-cascade configurations. These restrictions are discussed in the applications presented in Sec. IV. Hence, the incoming gusts (azimuthal component u'_θ only), in the case of a purely axial mean flow and annular cascade with zero stagger angle, can be written as

$$u'_\theta(x,r,t) = 2\sum_{i=1}^{N}\sum_{j=-M}^{M}\sqrt{\phi_{u_\theta u_\theta}(k_{x,i},k_{r,j})\Delta k_x \Delta k_r} \times \cos(k_{x,i}x + k_{r,j}r - \omega_i t + \varphi_{i,j}) \quad (1)$$

In Eq. (1), the mode amplitude is fitted by a von Kármán or Liepmann energy spectrum $\phi(k_x, k_r)$, defined by two parameters: the turbulence intensity T_u and the integral length scale Λ. Considering a frozen turbulence, the turbulent structures are assumed to be convected through the undisturbed upstream flow (mean velocity U_0), so that the angular frequency ω is related to the streamwise (axial) wave number k_x (aligned to the vane chord) by $k_x = \omega/U_x \cdot \varphi_{i,j}$. The random phase $\varphi_{i,j}$ associated to each mode $(i,\ j)$ is chosen between 0 and 2π. The synthetic turbulent field so obtained is solenoidal (divergence free), but if it is used with the full Euler equations, it is not a solution of the radial momentum equation due to a nonlinear term. Thus, the standard LEEs are solved in the CAA to prevent the generation of spurious oscillations.

As already discussed in the Introduction, although acoustic propagation might be directly assessed by CAA as done in Sec. III related to the spinning harmonic gust–cascade interactions, restrictions considered in Eq. (1) aiming at limiting the CAA domain to a single vane channel (using angular periodicity conditions) do not permit to capture the radiated sound field. It is practically obtained by a coupling to a FWH formulation (loading-noise term) using a Green's function valid for annular ducts and uniform axial mean flow [23,24], implemented in a Fortran90 code (FanNoise) developed at ONERA.

III. Validations on Academic NASA Benchmark Cases

Firstly, our numerical method has been validated against the third CAA benchmark cases proposed by NASA [15], devoted to the simulation of a swirling harmonic gust interacting with an annular cascade ($V = 24$ flat plates with chord $c = 1$ m) in an axial uniform mean flow ($M = 0.5$). This case was also successfully simulated by Hixon et al. [32]. The inflow-velocity disturbances using cylindrical coordinates (x, r, θ) are defined as

$$\begin{cases} u'_r(r,\theta,x,t) = 0 \\ u'_\theta(r,\theta,x,t) = A\ \cos[k_x x + m_g\theta + k_r(r - r_h) - \omega t] \\ u'_x(r,\theta,x,t) = -\frac{m_g}{rk_x}u'_\theta(r,\theta,x,t) \end{cases} \quad (2)$$

In Eq. (2), A is the gust amplitude, m_g is the gust azimuthal order, and the radial wave number is given by $k_r = 2\pi q/(r_t - r_h)$, in which q is an integer, and r_h and r_t are the inner and outer radii, respectively.

In the presence of spinning gusts [discarded in Eq. (1)], a suited axial component of disturbance velocity, u'_x, has to be also injected to ensure the divergence-free condition.

The following parameters are considered: $r_h = 24/4\pi(\mathrm{m})$, $r_t = 2r_h(\mathrm{m})$, $f_0 = \omega/2\pi = 177.5(\mathrm{Hz})$, $A = 0.1$, $U_0(\mathrm{m/s})$, and $m_g = 16$.

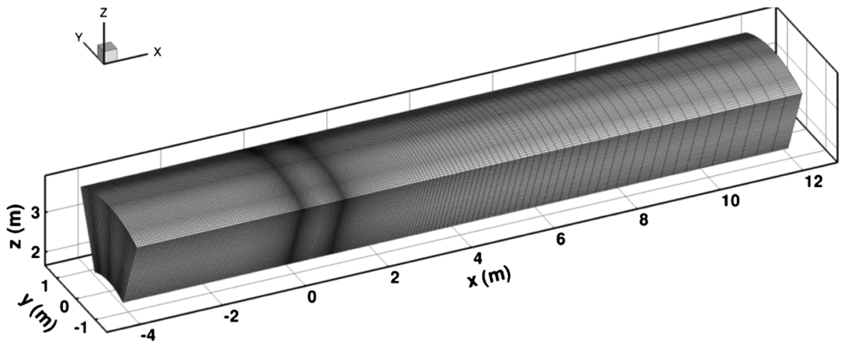

Fig. 1 Three-dimensional annular grid (three vane channels) used for the CAA benchmark.

Applying the well-known Tyler and Sofrin condition [33] ($m = nB - kV$, with $B = m_g$), a largely dominant acoustic mode with azimuthal order $m = -8$ is expected. Thus, the CAA domain can be restricted to a $2\pi/8$ angular sector covering three vane channels, and periodicity conditions can be applied in the azimuthal direction. A 3-D view of the mesh is shown in Fig. 1. The grid is extending from −4 chords (upstream) to 12 chords in the axial direction, and a very fine grid spacing of about 1/500 chord is imposed in the vicinity of the leading and trailing edges. Respectively, 370, 46, and 181 cells are used in the axial, radial, and azimuthal directions, which totalizes 3.2 million points. Because Tam's BCs [14] are not actually able to fully avoid reflections of outgoing spinning acoustic modes, a local stretching of the cells (with a coefficient equal to 1.03) associated to a sponge zone is applied at the exit (downstream) of the domain. A converged solution requires about 30 h over 120 processors.

Typical snapshots of the computed disturbance fields (tangential velocity and pressure) for the cases $q = 0$ and $q = 3$, repeated over a full revolution, are presented in Fig. 2. The expected dominant acoustic cut-on mode $m = -8$ is clearly identified, and the damping zone mentioned previously allows making the sound waves exit the domain without creating noticeable numerical reflections.

Radial distributions over the vane surface of the harmonic wall-pressure component ($f = f_0$) provided by the CAA are compared to available semi-analytical solutions of Schulten [17] in Fig. 3, for the case $q = 3$. The agreement is excellent, with only slight differences close to the trailing edge ($x = 0.9c$).

Finally, the modal amplitude and phase of the acoustic pressure obtained from a Fourier–Bessel transformation over a selected cross section at $x = 2c$ (one chord downstream of the cascade) are compared in Fig. 4 to the solutions of Namba and Schulten [15] for $q = 0$, 1, 2, 3, and cut-on modes (−8, 1), (−8, 2), (−8, 3). Again, a fairly good agreement is observed for all cases.

IV. Applications to Turbulence/Annular-Cascade Configurations

The previous single-harmonic gust simulations have been extended to broadband noise by considering a synthetic turbulent inflow obtained from a HIT spectrum. Two application cases are discussed next, considering purely axial and swirling mean flows, respectively.

A. Turbulence/Annular-Cascade Interaction in a Uniform Axial Mean Flow

1. *Experiment and Analytical Solution*

The first validation case is devoted to a turbulence–cascade interaction using a turbulence grid in a purely axial mean flow, related to an experiment proposed by ECL [18]. A picture of the anechoic open-jet wind tunnel with an outlet view of the model and a sketch of the test rig are shown in Fig. 5.

Two selected turbulence grids (T1, T2) with respective averaged turbulence intensity $T_u \approx 3.5\%$ and $T_u \approx 6\%$, and two cascades (C1, C2) with respective vane numbers $V = 49$ and $V = 98$ were

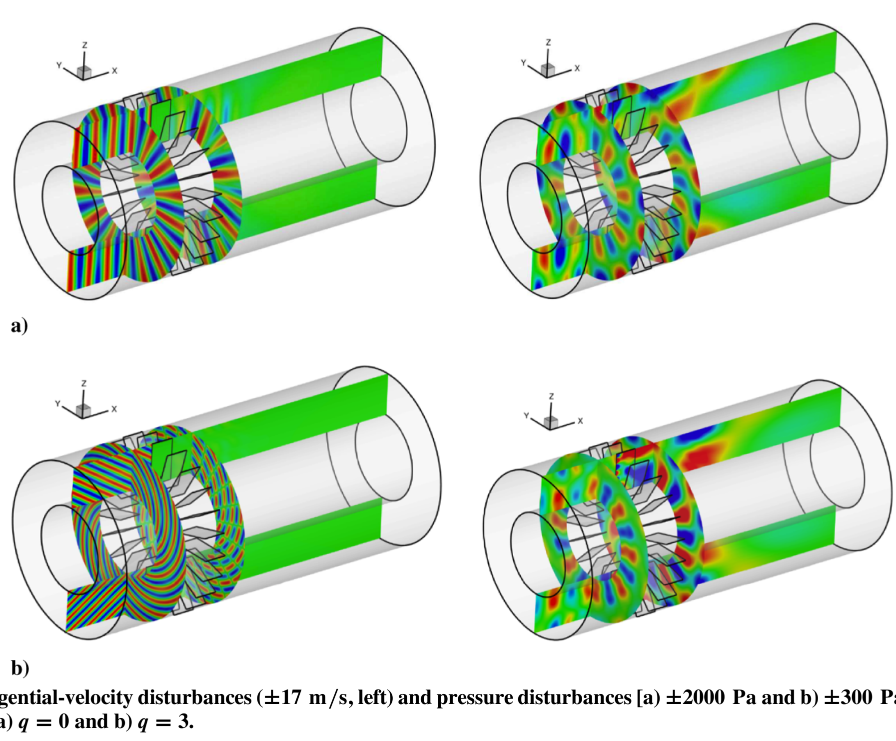

Fig. 2 Snapshots of tangential-velocity disturbances (±17 m/s, left) and pressure disturbances [a) ±2000 Pa and b) ±300 Pa, right] duplicated over a full revolution for cases a) $q = 0$ and b) $q = 3$.

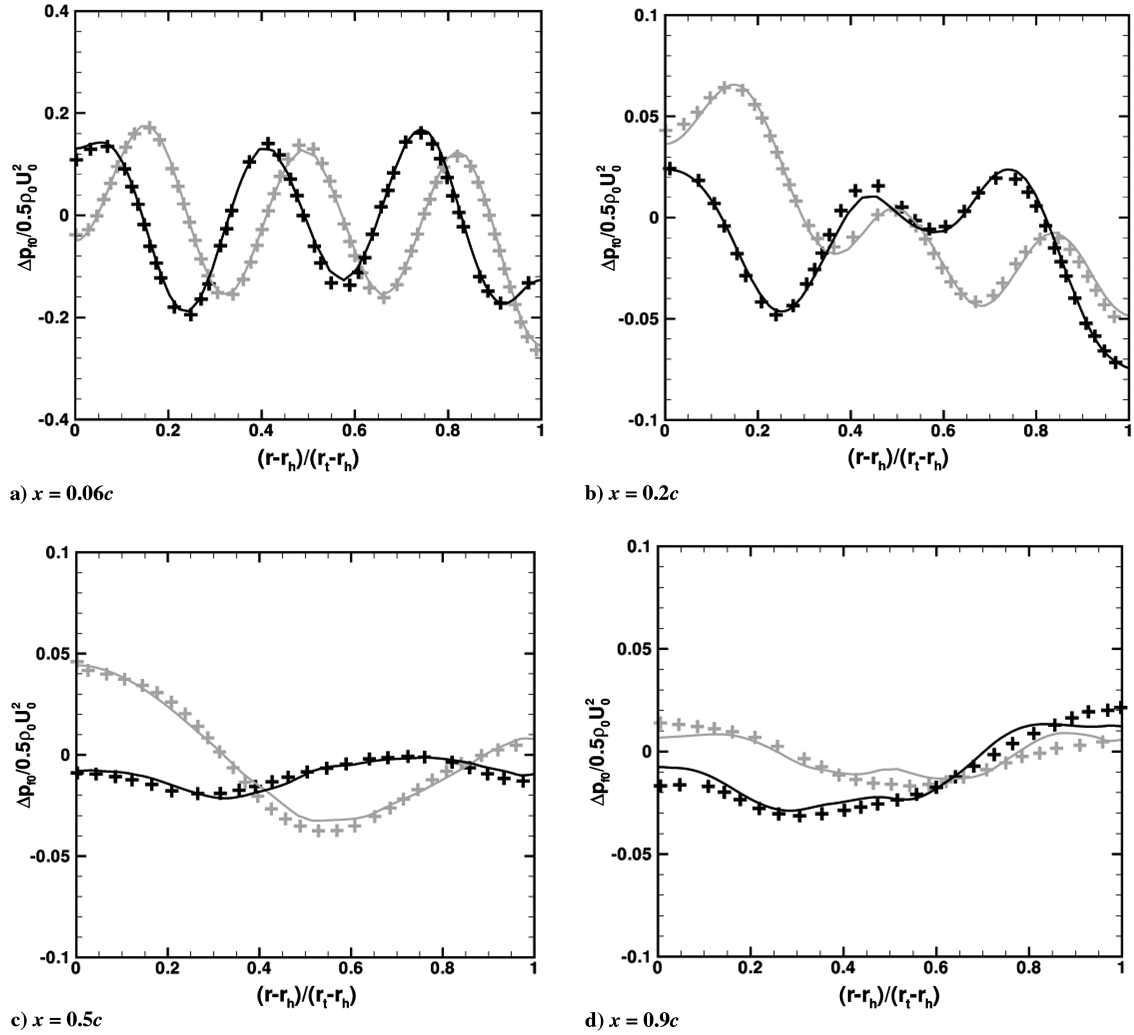

Fig. 3 Harmonic normalized pressure over the vane surface for $q = 3$: CAA results (—) compared to Schulten results (+) [15]; real part (light) and imaginary part (dark).

investigated. The flat-plate vanes have an $L = 80$ mm span, a $c = 25$ mm chord, and a $\chi = 16.7$ deg stagger angle (with a 0 deg angle of attack). The inner and outer radii of the annular duct are, respectively, $r_h = 150$ mm and $r_t = 230$ mm, and the mean (axial) velocity is $U_0 = 80$ m/s. The T1 and T2 grids gave an estimated integral length scale Λ around 20 mm when fitting the hot-wire measurements to the Liepmann HIT model.

The two-wave-number Liepmann spectrum expressed in cylindrical coordinates in the x-duct frame writes

$$\phi_{u_\theta u_\theta}(k_x, k_r) = \frac{3\overline{u_\theta'^2}}{4\pi} \frac{k_x^2\Lambda^2 + k_r^2\Lambda^2}{(1 + k_x^2\Lambda^2 + k_r^2\Lambda^2)^{5/2}} \tag{3}$$

In Eq. (3), the turbulent upwash velocity u_θ' is related to the turbulence intensity T_u as $\overline{u_\theta'^2} = T_u^2 U_0^2$. The CAA simulations have been focused on the T2–C1 and T2–C2 cases, for which the main parameters are summarized in Tables 1 and 2. It can be noticed that the turbulence-flow characteristics generated by the turbulence grid are slightly modified when changing the cascade vane number. (The present values for cascade C2 used here are expected to be more representative than those reported in [18], in which the same values were considered for grids C1 and C2.)

For the sake of simplicity, the stagger angle is set to zero in the simulations because its effect on turbulence–airfoil noise, for small values, is known to be negligible. Indeed, calculations of sound power spectra in the outlet duct issued from the Amiet-based code developed by Reboul et al. [23] and Reboul [24] (considering an isolated-airfoil-response model and a Green's function valid for annular ducts), and setting $\chi = 0$ deg or $\chi = 16.7$ deg provide almost identical results (see Fig. 6). This Amiet-based formulation is detailed in the Appendix. Furthermore, the incoming turbulence can be restricted to parallel gusts [$k_r = 0$ in Eqs. (1) and (3)], as done in Amiet's [1] theory and suggested in [24] for turbofans with span-to-chord ratio $L/c > 3$. This assumption was also verified numerically by Clair et al. [8] for turbulence–airfoil simulations. As explained in [8], this is simply achieved in the CAA by setting $\Delta k_r = 2\pi/L$ in Eq. (1).

The Amiet-based results are compared to the solutions obtained by Posson and Roger [18] and Zhang et al. [25] in Fig. 7, and to the experiment too. The T1–C1 case was recently investigated by Zhang et al. [25] who addressed a quite relevant solution based on the lifting-surface method of Schulten [17], generalized to broadband noise. Zhang et al.'s result for the T1–C1 case has been extrapolated to the T2–C1 case in Fig. 7b by simply applying a frequency depending correction factor that is equal to the ratio of the corresponding Liepmann spectra. For both cases, the three predictions are reasonably close with a 3–4 dB overestimate of Reboul's results [24] compared to those of Zhang et al., which can be partly attributed to cascade effects too, neglected in Amiet's [1] isolated-airfoil theory, although the Amiet-based predictions better fit the experiment. (The low-frequency hump beyond 500 Hz visible on the experimental spectra has to be related to an additional noise caused by installation effects [18].) The 3-D lifting-surface method, expected to be the most rigorous one, provides rather similar results to the quasi-3-D cascade model of Posson and Roger [18] in the high-frequency range, whereas the Power Watt Level (PWL) spectrum of Reboul displays a lower level attenuation slope.

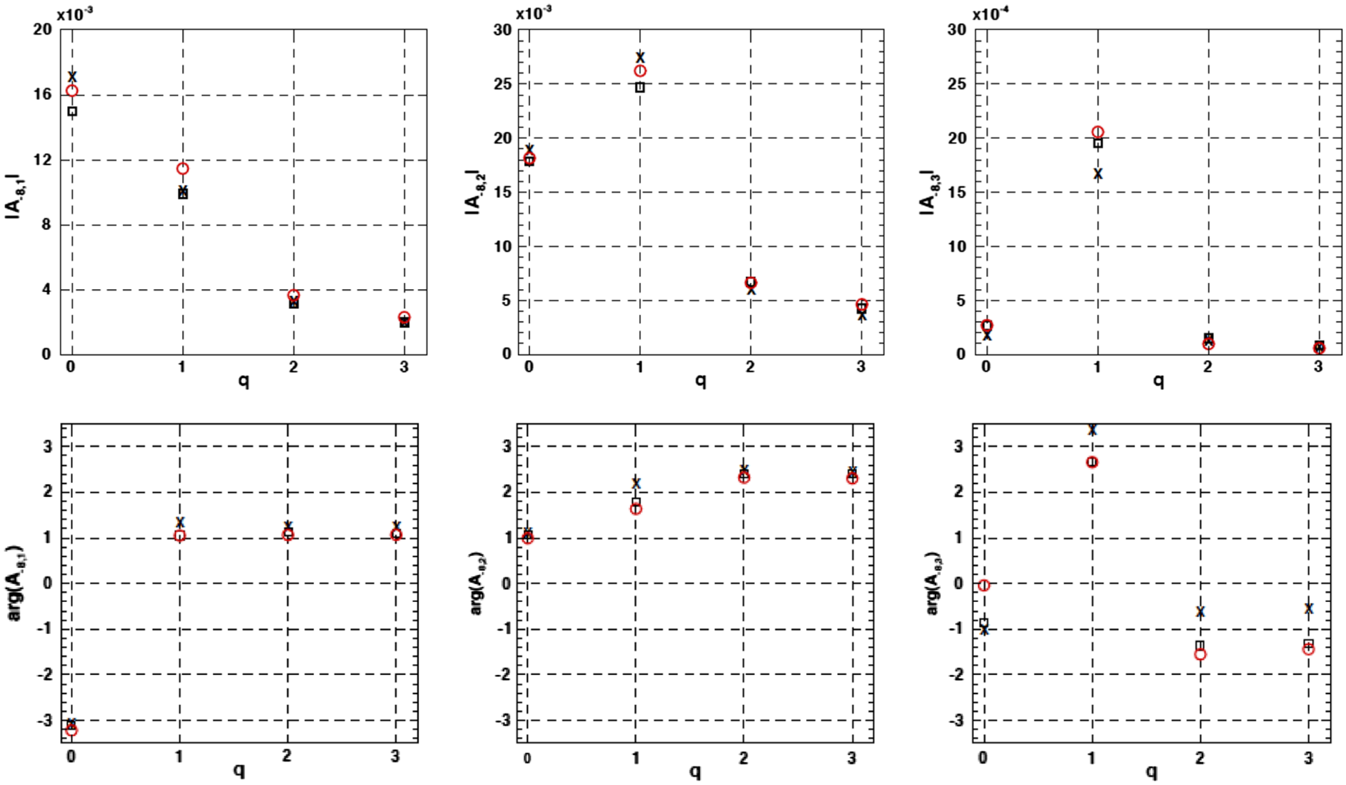

Fig. 4 Modal amplitude (top) and phase (bottom) issued from a Fourier–Bessel transform at $x = 2c$: $m = -8$ ($n = 1$–3) and $q = 0, 1, 2, 3$; CAA results (○) compared to Schulten (□) and Namba (×) [15].

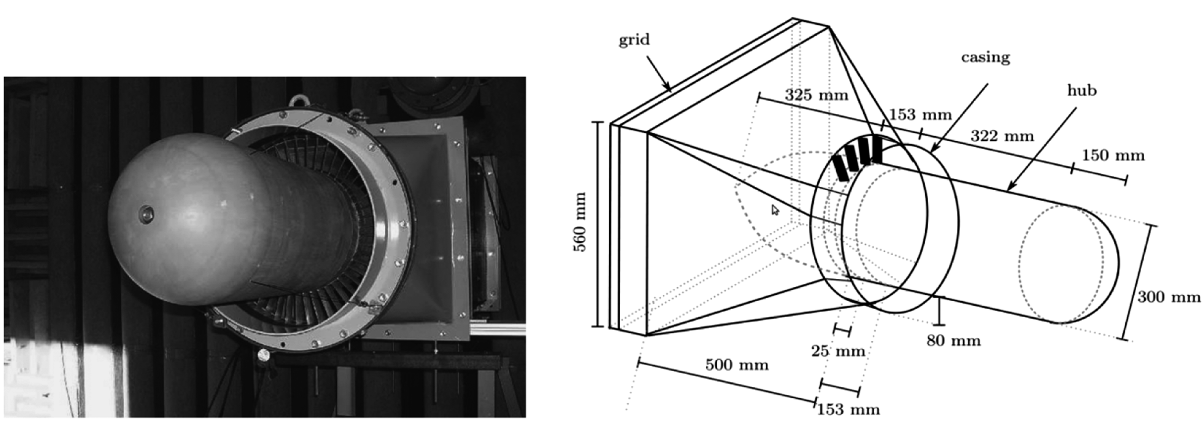

Fig. 5 ECL open-jet anechoic wind-tunnel experiment (left) and sketch of the rig (right).

2. *Mesh Generation*

The use of a simplified turbulence-spectrum representation, $\phi(k_x, 0)$, without azimuthal dependence, allows us to limit the CAA domain to a single vane channel by applying suitable periodicity conditions in the angular direction (and so to greatly reduce the CPU costs). Thus, the CAA domain is restricted to a $2\pi/V$ sector leading to a 3-D grid of about 1.5 million cells. The CAA grid characteristics are summarized in Table 3. The mesh for cascade C2 ($V = 98$) is simply achieved by reducing by half the angular spacing used for C1 so that the number of grid points in each direction remains the same. The 3-D and section views of the CAA grids are shown in Fig. 8. The synthetic turbulent inflow is injected for frequencies ranging from 300 to 5000 Hz, with a frequency resolution $\Delta f = 100$ Hz. Hence, a complete period $T = 1/\Delta f$ is achieved after 85,000 time iterations, requiring about 27 h over 64 processors for the two cases, and converged statistics are obtained after only two periods.

Table 1 Annular-cascade geometry and flow considered in the CAA

Parameter	Values
r_h, mm	150
r_t, mm	230
c, mm	25
L, mm	80
χ, deg	0
U_0, m/s	80

Table 2 Radially averaged turbulence data used in the CAA

Grid cascade	T1–C1 ($V = 49$)	T1–C2 ($V = 98$)	T2–C1 ($V = 49$)	T2–C2 ($V = 98$)
T_u, %	3.6	3.4	6	5.5
Λ, mm	17.6	22	20	25.6

Although Amiet's [1] theory is only valid for an isolated airfoil, cascade effects should be taken into account here by the use of periodicity conditions, traducing the influence of adjacent vanes on the aerodynamic response of the airfoil. However, the restriction to planar gusts [which is similar to setting $m_g = 0$ in Eq. (2)] does not allow anymore to assess the acoustic response directly, as done with harmonic gusts in Sec. III. Indeed, only interaction modes $m = \pm kV$ can be created, and as turbulence–airfoil interactions occur in phase for all vanes, interference effects between dipole sources of adjacent vanes lead to a quasi-null radiated field. This point is illustrated in Fig. 9, showing snapshots of azimuthal-velocity disturbances (Fig. 9, left) and pressure disturbances (Fig. 9, right) over a 3-D annular slice corresponding to the CAA domain duplicated over three angular sectors. The planar shape of the multiharmonic gusts is clearly highlighted, as well as the dipolar source response of each vane, giving rise to a noise cancellation in the upstream and downstream directions due to destructive interference effects. Anyway, the fluctuating wall pressure over the vane surface is expected to be reliable, and the radiated sound field can be computed by means of a FWH analogy. This is practically achieved by chaining the CAA output to an in-house code solving the loading-noise term of the FWH formulation (with an in-duct modal Green's function) written in the frequency domain.

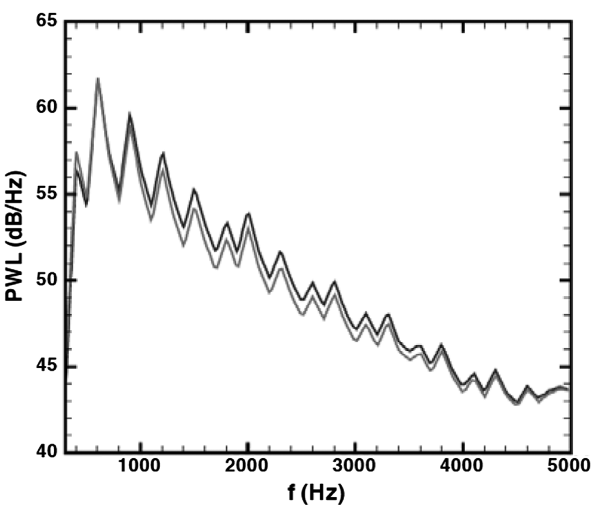

Fig. 6 Power Watt Level spectra (dB/Hz) in the outlet duct provided by the Amiet-based calculation on T2–C1 case and setting $\chi = 16.7$ deg (light) or $\chi = 0$ deg (dark).

Table 3 CAA grid characteristics

Parameter	Values
N_x	373
N_r	51
N_θ	81
Axial extent, m	$-0.1 < x < 0.25$
Radial extent, m	$0.15 < r < 0.23$
Azimuthal extent, rad	$-\pi/49 < \theta < \pi/49$
	$-\pi/98 < \theta < \pi/98$

The rms surface pressure over the vane is plotted in Fig. 10 showing an expected source concentration in the leading-edge region. Chordwise rms pressure profiles (normalized by $\rho_0 U_0^2$), computed by the CAA at hub (light), midspan (medium), and casing (dark) locations, are compared to the Amiet-based (isolated airfoil) solution in Fig. 11. A reasonably good agreement can be observed, but the levels of the computed profiles are slightly below the Amiet-based solution: this might be attributed to cascade effects that are taken into account in the CAA.

Finally, in Fig. 12, the PWL spectrum provided by the CAA–FWH calculation is compared to Zhang et al.'s [25] semi-analytical solution, and to the measurements for which corrected data (partial filtering of extra source contribution suggested in [17]) are also addressed. The numerical prediction is very close to Zhang et al.'s solution, both spectra revealing an accurate capture of the peaks even if the levels are a little bit higher compared to the corrected experiment. Furthermore, the numerical prediction displays a slightly lower level attenuation slope that better fits the experiment beyond 2000 Hz compared to the lifting-surface method. The PWL reduction of about 3 dB compared to the Amiet-based solution of Reboul [24] (Fig. 8, right) is in accordance with the wall-pressure analyses discussed in Fig. 11.

3. *T2–C2 Simulation*

The second simulation has been performed on the T2–C2 case with similar analyses. A comparison of the pressure profile along the vane chord at midspan is presented in Fig. 13a, revealing a much lower amplitude of the cascade C2 response compared to C1. The estimated PWL spectrum obtained by the coupling with the FWH integral (and applying a noncoherent sum over 98 vanes instead of 49) is compared to the previous result in Fig. 13b. Surprisingly, the cascade C2 is found to be less noisy than C1, suggesting a very strong cascade effect. Regarding the cascade C2 geometry, the intervane distance at midspan is equal to 12 mm, which is about half the size of the turbulence integral length scale. For this reason, the unusual intense

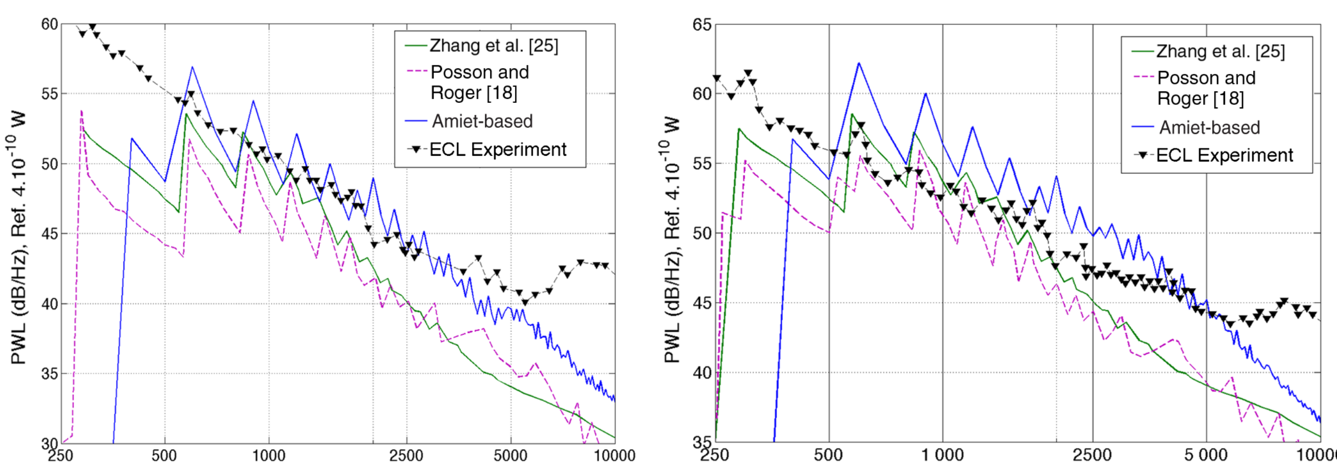

Fig. 7 Comparison of outlet PWL spectra obtained by three different calculation methods applied to the ECL experiment (raw measurements) for the T1–C1 (left) and T2–C1 (right) cases.

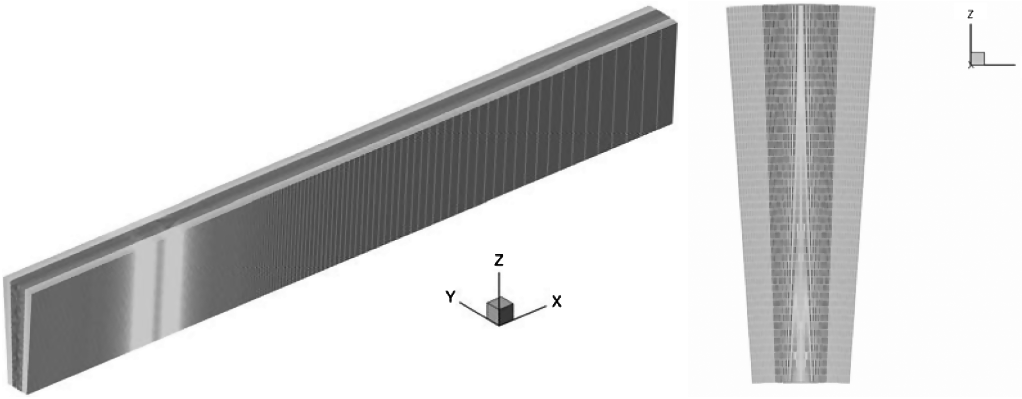

Fig. 8 Three-dimensional view (left) and section view (right) of CAA grids for cascade C1 (light) and C2 (dark) A.3 T2–C1 simulation.

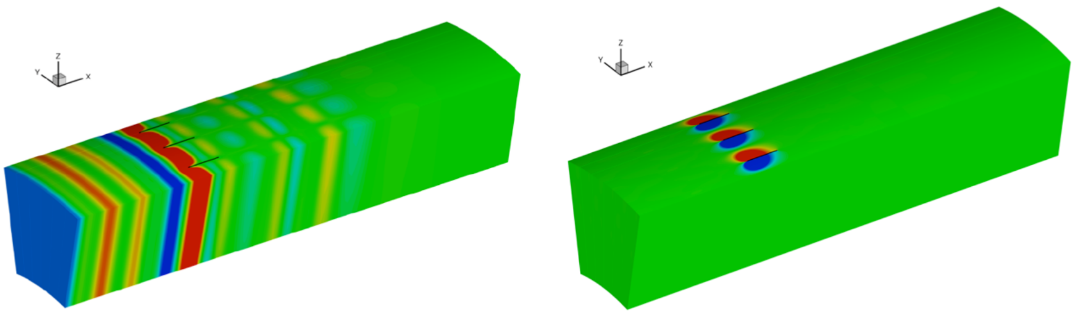

Fig. 9 Snapshot of azimuthal-velocity disturbances (± 2.5 m/s, left) and pressure disturbances (± 100 Pa, right) duplicated over three angular sectors for the case T2–C1.

acoustic coupling between vanes is suspected including correlation effects between adjacent vanes (whereas vanes are assumed to be fully uncorrelated in the FWH formulation). It is also important to notice that, although the turbulence intensity is almost the same, the mean value of the turbulence integral length scale for the T2–C2 case ($\Lambda = 25.6$ mm) is 25% higher than for the T2–C1 case ($\Lambda = 20$ mm), giving rise to a significant modification of the cascade response (independently to the vane-number ratio). Thus, the PWL amplifications from cascades C1 to C2 provided by the Amiet-based predictions (neglecting cascade effects) plotted in Fig. 14 do not highlight the expected $10\log(V)$ law with isoturbulence (dashed line), under the present experimental conditions.

The PWL spectrum numerically obtained is then compared to Zhang et al.'s [25] solution and to the experiment in Fig. 15. Both predictions are found to be in a rather good agreement, although the PWL issued from the lifting-surface method is 3–4 dB higher in the low-frequency range (300–1000 Hz). The two solutions become almost identical beyond 1.5 kHz, whereas they are drifting away from the measurements that are displaying a much lower attenuation slope. On the other hand, the ONERA prediction seems to better fit the measurements (more particularly the corrected data) up to 1.5 kHz.

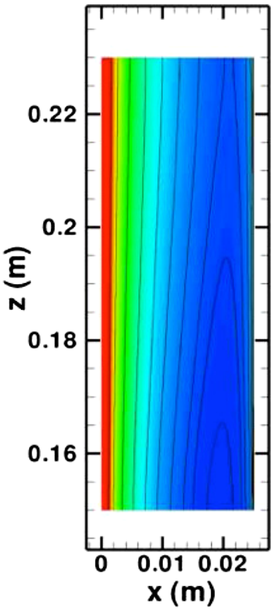

Fig. 10 RMS vane-surface pressure (0–300 Pa).

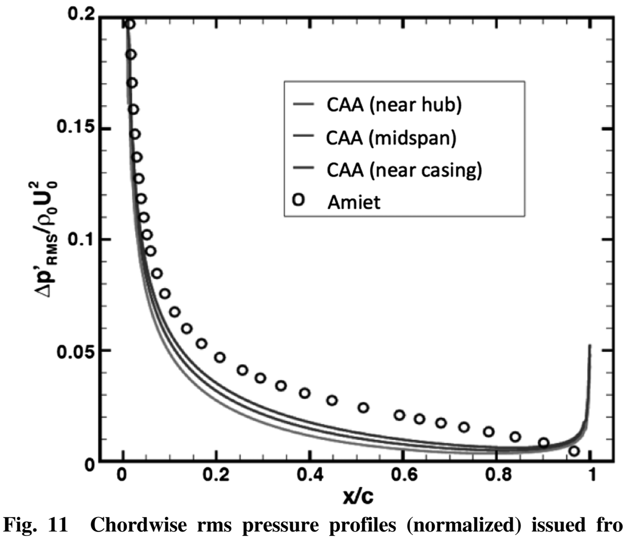

Fig. 11 Chordwise rms pressure profiles (normalized) issued from CAA and Amiet [1].

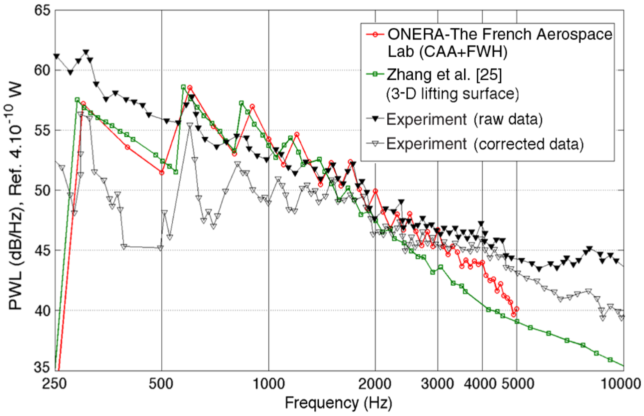

Fig. 12 Outlet duct PWL spectra provided by CAA + FWH, semi-analytical method (Zhang et al. [25]) and compared to experiments (raw and corrected measurements) for the T2–C1 case.

Finally, the PWL amplifications/attenuations (adopting a linear scale for frequency) provided by the calculations are compared to those deduced from the measurements in Fig. 16. An important dispersion of the results with significant-level differences can be observed, and no method is actually able to match the experimental results (the Amiet-based solution being the closer one to the corrected data, which is not realistic and makes these corrections not fully reliable). However, the three predicted spectra exhibit similar shapes, with a strong increase at lower frequencies, and then tending to an asymptotic behavior at high frequency. Zhang et al.'s [25] predictions display a quasi-null PWL amplification from 1 to 3 kHz, and then an attenuation (reaching −2 dB), which tend to confirm the trend of our numerical results, even if we predict a higher attenuation with a level shift within 1.5–3.5 dB.

4. Complete Turbulence Spectrum ($k_r \neq 0$)

To check our numerical predictions, the previous simulations have been run again by considering the complete turbulence spectrum given by Eq. (1), including the radial wave numbers (k_r). For that purpose, as suggested in the conclusions of [11], the code sAbrinA.v0 has been modified to speed up the turbulent-flow-generation process by externalizing part of the source terms (read from an input data file) involved in Tam's inflow BC [8,14]. Only source-term derivatives of Tam's BCs are calculated in the code. By this way, the CPU time involved for the generation of the turbulence is negligible compared to the CAA, so that the total CPU time for the complete spectrum ($k_r \neq 0$) is comparable.

The radial-wave-number spacing Δk_r is set equal to $2\pi/L$ ($L = 80$ mm), and the maximum number of radial modes [$2M$ in Eq. (1)] is related to the CAA grid density (in the spanwise direction)

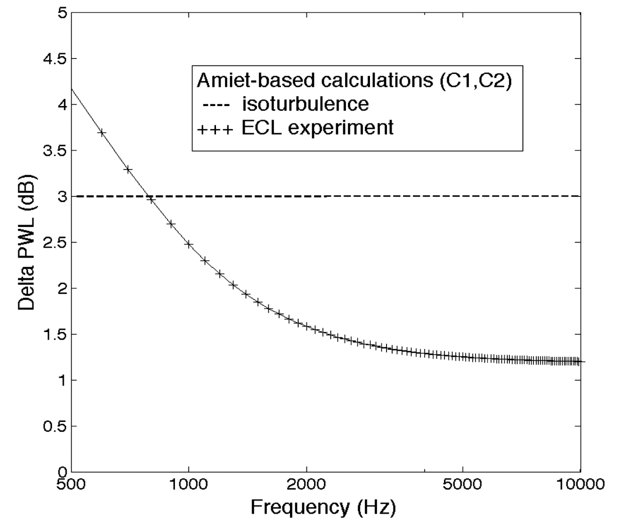

Fig. 14 PWL amplification (dB) from cascade C1 to C2 obtained from Amiet-based ONERA code considering isoturbulence or ECL experiment conditions (T2 grid).

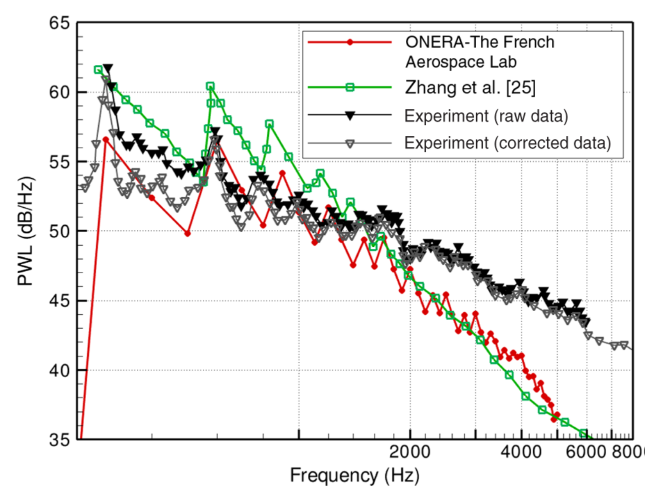

Fig. 15 Outlet duct outlet PWL spectra provided by CAA + FWH (ONERA), semi-analytical method (Zhang et al. [25]) and compared to experiments (raw and corrected measurements) for the T2–C2 case.

at the inflow boundary. Here, 50 regular radial planes are used, so that 26 radial modes ($2M$ modes plus parallel gust) are imposed, referring to the Shannon criterium. Here, as $U_r = 0$ and $u'_r = p' = 0$ for the

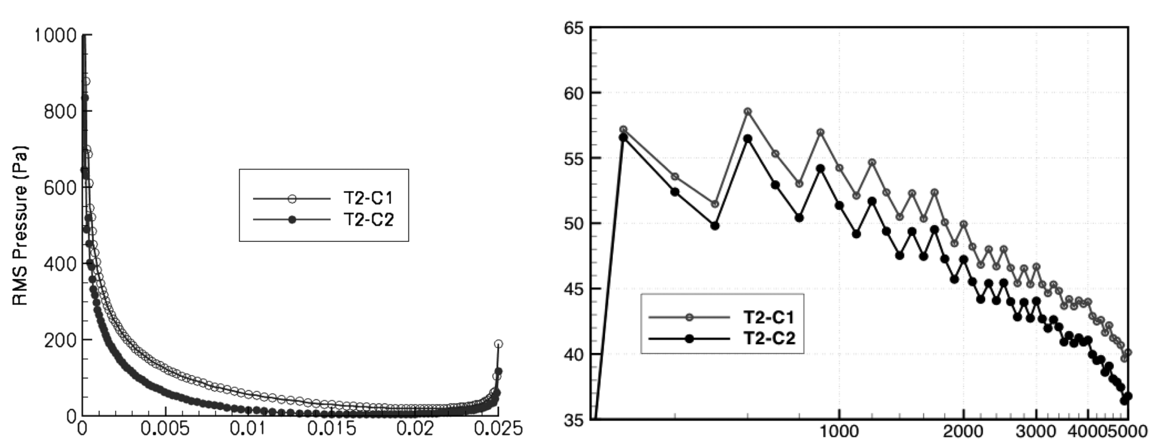

a) RMS wall pressure along the chord (at midspan) **b) PWL spectra in the outlet duct**

Fig. 13 Comparison of numerical-simulation results between the T2–C1 (light) and T2–C2 (dark) cases.

synthetic turbulent field, there are no terms involving radial derivatives in the LEE, and thus, the 10-points-per-wavelength criterion is not limiting in this direction during the convection of the incoming perturbations. However, one should note that the direct acoustic radiation from the vanes (not solved with the present method) might not be accurately captured by the CAA for the higher radial modes. As for previous computations, convergence is achieved after two complete periods, and the total required CPU time (54 h over 64 processors) is almost the same. Typical 3-D snapshots of azimuthal-velocity and pressure disturbances are shown in Fig. 17. In comparison to Fig. 9 (left), the synthetic turbulent flow (Fig. 17, left) provided by the present stochastic model highlights random patterns in both axial and radial directions. Here, again, the pressure disturbance field reveals a dipole source concentrated at the leading edge of the vane and a quasi-null radiated sound field (for the same reason discussed before). It can be noticed that the pressure levels are much lower than for the T2–C1 case. Moreover, some spurious spots can be observed near the bottom corner of the CAA domain exit, probably due to remaining numerical reflections. In Fig. 18a, the rms vane-pressure map predicted using the present synthetic turbulence (including oblique gusts) for the T2–C2 case is compared to the one

Table 4 Swirling mean-flow and stagger-angle values

r, m	$\bar{r}$	M_θ	M_x	χ, deg
0.99	0.75	0.2604	0.4681	29.1
1.32	1.00	0.2500	0.4330	30.0
1.65	1.25	0.2563	0.3949	33.0

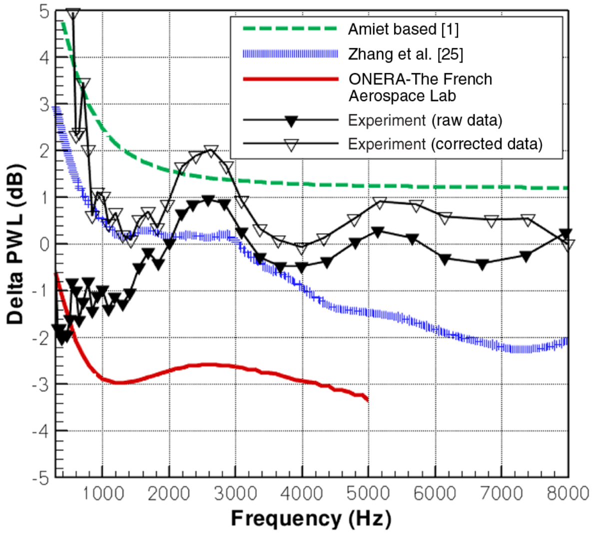

Fig. 16 PWL amplification or attenuation (in dB) issued from calculations and measurements related to the T2–C1 and T2–C2 cases.

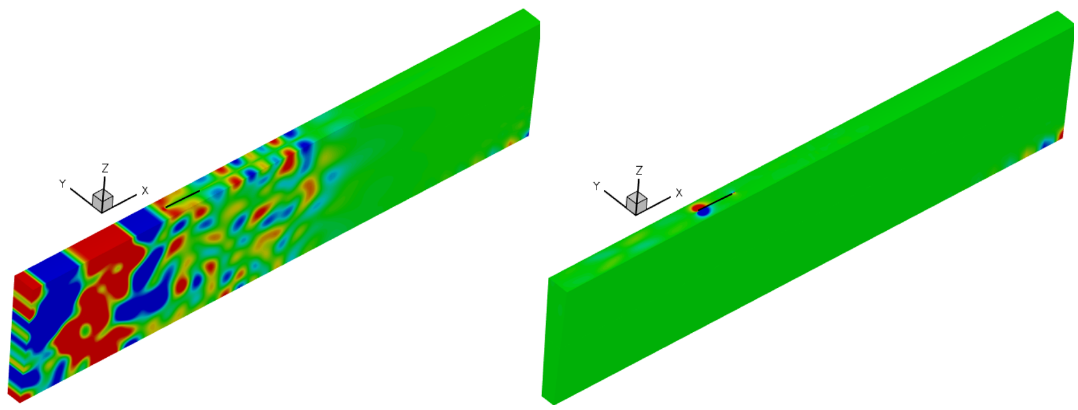

Fig. 17 Snapshots of azimuthal-velocity disturbances (±2.5 m/s, left) and pressure disturbances (±25 Pa, right) for the case T2–C2 using synthetic turbulence with radial wave numbers.

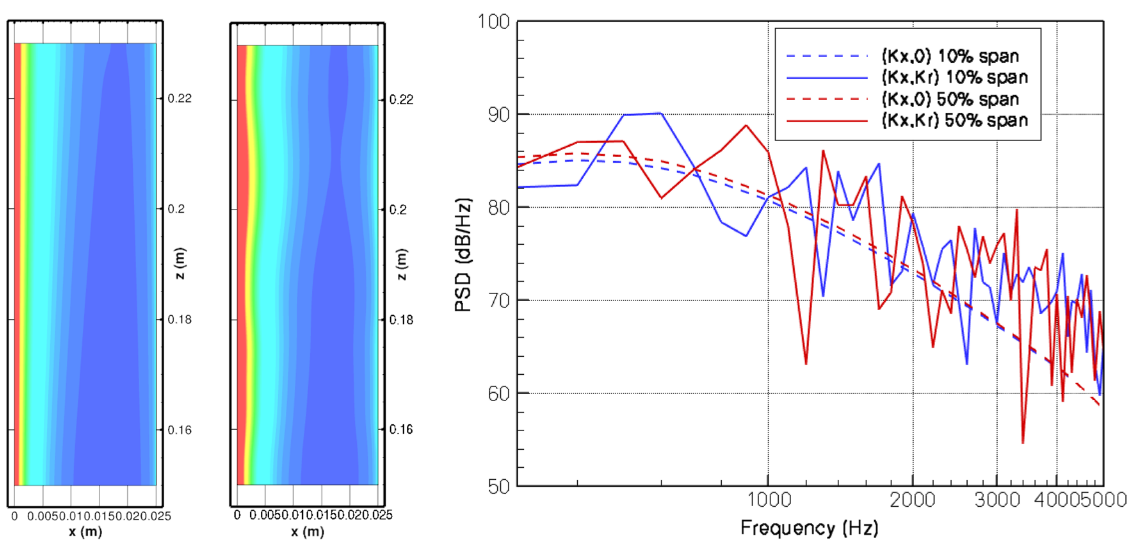

a) RMS vane surface pressure (0-300 Pa) **b) Pressure PSD (dB/Hz) near the leading edge**

Fig. 18 Comparison of CAA predictions using synthetic turbulence without [a) left, b) dashed lines] and with [a) right, b) solid lines] radial wave numbers for the T2–C2 case.

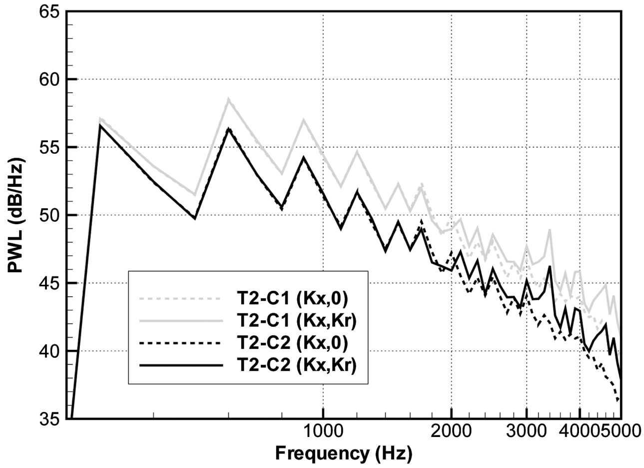

Fig. 19 Comparisons of PWL spectra in the outlet duct provided by CAA + FWH computations using (k_x, k_r) turbulence (solid lines) and $(k_x, 0)$ turbulence (dotted lines) for the T2–C1 (light) and T2–C2 (dark) cases.

obtained using parallel gusts (Fig. 18a, left), showing very similar patterns and levels despite a slightly more oscillating solution in the spanwise direction (Fig. 18a, right). The pressure PSDs near the leading edge of the vane for two radial positions (10 and 50% of the span) are compared in Fig. 18b. The solutions obtained with the complete 2-D turbulence spectrum (solid lines) display high oscillations compared to the ones issued from the turbulent inflow restricted to axial modes (dashed lines). This is due to the interference effects between radial modes and the fact that no averaging (that would require several runs with different sets of random phases) has been realized. Note that statistical errors could be simply reduced by integrating the PSD levels over consecutive spectral bands, as done in [8]. Anyway, the fluctuating levels of the spectra seem to oscillate around a mean value that roughly fits the smooth solution, although higher levels at high frequencies can be observed.

Finally, the PWL spectra in the outlet duct predicted by the coupling with an FWH integral for both approaches are compared in Fig. 19 for the two cases T2–C1 (light) and T2–C2 (dark). Despite the oscillations present in the pressure PSD, the radiated PWL spectra using the complete spectrum (k_x, k_r) turbulence spectrum (plotted in solid lines) are almost identical to the previous ones (in dotted lines), excepted a slight increase of the levels beyond 2 kHz, consequently to the PSD level increase observed in Fig. 18b. Thus, the cascade effects highlighted in Fig. 16 are not expected to be modified.

These results tend to validate our numerical method with parallel-gust restriction for this cascade configuration in a uniform axial mean flow. The more realistic case of a swirling mean flow is discussed in the next section.

B. Turbulence/Annular-Cascade Interaction in a Swirling Mean Flow

The second application case concerns a benchmark proposed by Atassi and Vinogradov [20], related to an annular grid of $V = 45$ unloaded flat plates with 160 mm chord in a swirling mean flow. This has been also investigated by Hixon et al. [32], but considering only a single-harmonic spinning gust (tone noise), whereas we focus here to an HIT inflow condition (broadband noise). The vanes are twisted with a suited stagger angle χ varying along the span and adjusted, so that the angle of attack remains equal to zero (local chord aligned with the streamlines). The characteristics of the annular duct are $r_h = 0.99$ m and $r_t = 1.65$ m. The swirling mean flow is imposed by an axial and azimuthal component (the radial component being set to zero). The azimuthal Mach number is defined as (setting $\Omega = \Gamma = 0.125$)

$$M_\theta(\bar{r}) = \Omega\bar{r} + \frac{\Gamma}{\bar{r}} \tag{4}$$

Using Crocco's equation and neglecting the entropy and enthalpy variations, the axial Mach number can be written as [34]

$$M_x(\bar{r}) = \sqrt{M_x^2(r_{\mathrm{mid}}) - 2[\Omega^2(\bar{r}^2 - 1) + 2\Omega\Gamma\,\ln(\bar{r})]} \tag{5}$$

The mid-span radius r_{mid} is equal to 1.32 m, which corresponds to a total Mach number equal to 0.5 at this position.

The main parameters are summarized in Table 4, in which $\bar{r}$ is the radius normalized by its midspan value r_{mid}.

The mean static-pressure field is derived from the radial momentum equilibrium:

$$p(\bar{r}) = p_\infty\left\{1 + (\gamma-1)\left[\left(\frac{\bar{r}^2-1}{2}\right)\left(\Omega^2 + \frac{\Gamma^2}{\bar{r}^2}\right) + 2\Gamma\Omega\ln(\bar{r})\right]\right\}^{\gamma/(\gamma-1)} \tag{6}$$

In Eq. (6), $\gamma = 1.4$ and $p_\infty = 101{,}986$ Pa. The mean density field is defined as $\rho(\bar{r}) = \rho_\infty[p(\bar{r})/p_\infty]^{1/\gamma}$, and the stagger angle (set equal to the inflow angle) is deduced as $\chi(\bar{r}) = \arctan[M_\theta(\bar{r})/M_x(\bar{r})]$.

The radial profiles of the three fields $M_x(\bar{r})$, $M_\theta(\bar{r})$, $\chi(\bar{r})$ so obtained are plotted in Fig. 20.

The Cartesian coordinates $(x_\varsigma, y_\varsigma, z_\varsigma)$ of a point ς along a vane in the curvilinear frame (ξ, η, r) sketched in Fig. 21 can be expressed as

$$\begin{cases} x_\zeta(r) = \xi\,\cos[\chi(r)] \\ \alpha_\varsigma(r) = \frac{\xi\,\sin[\chi(r)]}{r} \\ y_\zeta(r) = r\,\sin[\alpha_\varsigma(r)] \\ z_\zeta(r) = r\,\cos[\alpha_\varsigma(r)] \end{cases} \tag{7}$$

A 3-D representation of the annular grid with colored stagger angle varying from 29 to 33 deg is shown in Fig. 22, and the CAA grid made of about 1.4 million points (limited to a single vane channel) is visualized in Fig. 23. The computation parameters are summarized in Table 5.

Because of the fact that the vane chord is not aligned with the duct axis anymore, the synthetic turbulent inflow injected into the CAA

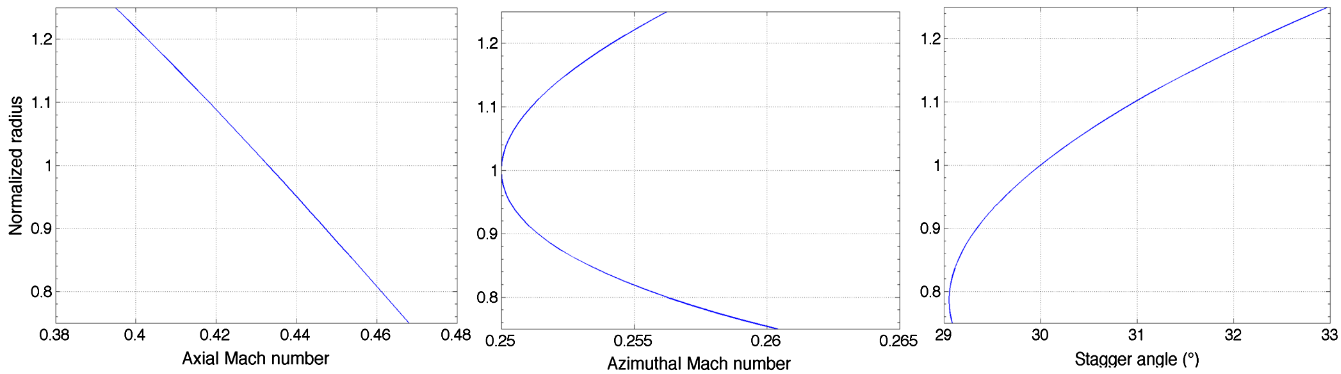

Fig. 20 Radial profiles of axial (left) and azimuthal (middle) Mach number, and stagger angle (right).

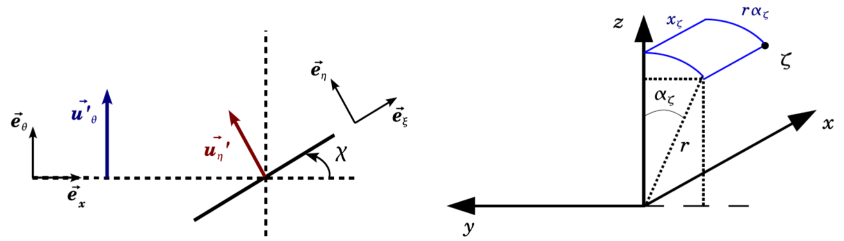

Fig. 21 Local frames attached to the duct and to the vane (left), and Cartesian coordinates related to curvilinear points (right).

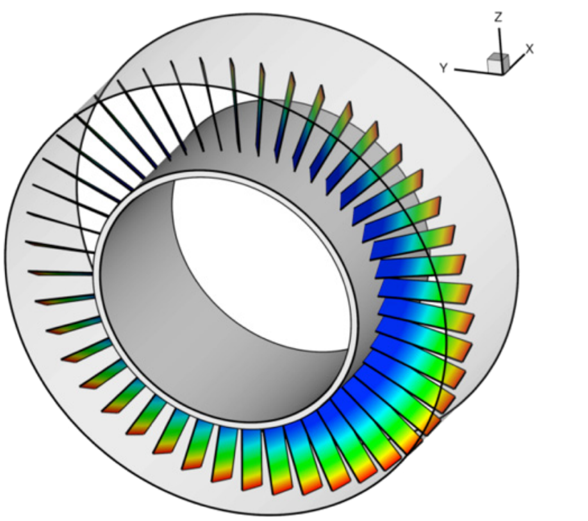

Fig. 22 Three-dimensional representation (full revolution) of the cascade with colored stagger angle between 29 and 33 deg.

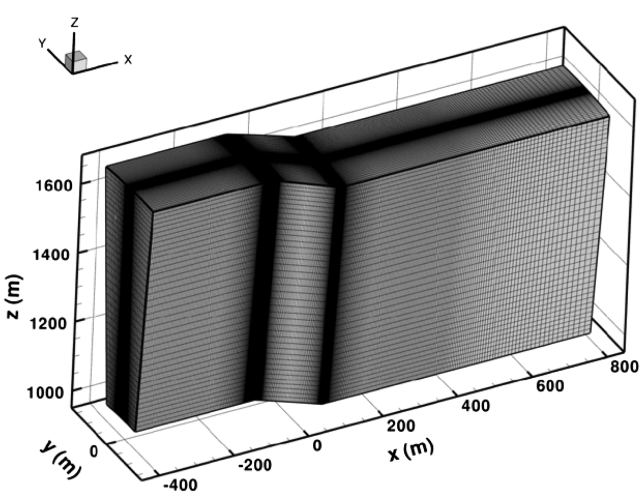

Fig. 23 CAA 3-D grid of a single vane channel of the annular grid.

frame with Cartesian coordinates (x, y, z) related to the duct cylindrical coordinates(x, r, θ) has to be expressed with respect to the local vane curvilinear coordinates (ξ, η, r). Hixon et al. [32] suggest a suited vortical-gust-boundary-condition formulation at the inflow boundary in the CAA frame implemented in the BASS code from the NASA Glenn Research Center, but it would require to expand the synthetic turbulence over angular modes, and so to mesh all the vanes over a 360 deg domain. Another strategy is proposed here to still limit the CAA grid to a single vane channel. Thus, restricting again to the parallel gusts ($k_r = 0$) and introducing the stagger angle χ, the velocity disturbances of Eq. (1) are rewritten as

Table 5 CAA grid characteristics

Parameter	Values
N_x	417
N_r	41
N_θ	85
Axial extent, m	$-0.4 < x < 0.8$
Radial extent, m	$0.99 < r < 1.65$
Azimuthal extent, rad	$-\pi/45 < \theta < \pi/45$

$$\begin{cases} u'_\theta(x,r,\theta,t) = 2\sum_{i=1}^{N} A_i \cos(k_{x,i}x - \omega_i t + \varphi_i) \\ A_i = \frac{\sqrt{\phi_{u_\eta u_\eta}(k_{\xi,i},0)\Delta k_\xi \Delta k_r}}{\cos[\chi(r)]} = \frac{\sqrt{\phi_{u_\eta u_\eta}(k_{x,i}\cos[\chi(r)],0)\Delta k_x \cos[\chi(r)]\Delta k_r}}{\cos[\chi(r)]} \end{cases} \quad (8)$$

The wave numbers k_x and k_ξ are linked by $k_\xi = k_x \cos\chi$. As $x_\varsigma = \xi_\varsigma \cos\chi$, the phase term $k_x x$ in Eq. (3) is actually equal to $k_\xi \xi$ at the vane wall. One should note that, by projection of u'_θ, a component u'_ξ will be also added to the upwash component u'_η. However, these fluctuations are sliding along the chord and are not expected to generate any sound.

As for the previous case, the restriction to parallel gusts [$k_r = 0$ in Eq. (3)] to reduce the CPU cost is justified by the practical requirement $L/c \geq 3$. However, this simplification proposed by Amiet [1] for isolated airfoils and checked by Reboul et al. [23] and Reboul [24] for ducted fans is valid for nonvarying inflow conditions along the span, which is no more true here. The parallel-gust restriction in the CAA then might be questionable and will be discussed next.

As defined by Atassi and Vinogradov [20], the turbulence is modeled using the Liepmann TKE spectrum, with constant parameters $T_u = 1.8\%$ and $\Lambda \approx 42$ mm. Harmonic gusts are injected with a frequency spacing $\Delta f = 100$ Hz up to $f_{\max} = 3300$ Hz. About 16,500 time iterations are required to simulate a complete period, and a converged result is reached after two periods, requiring only 12 h over 64 processors.

The 3-D snapshot views of azimuthal-velocity and pressure disturbances can be visualized in Fig. 24, left and right, respectively. As explained previously, the wave fronts are almost normal to the duct axis and not to the vanes. The wave-front lean traduces the radial variations of the mean flow. The wall-pressure distributions provided by the CAA over lower and upper vane sides are plotted in Fig. 25 (right), for several spanwise positions, and compared to the Amiet [1] solution. A rather good agreement can be observed, despite a nonsymmetrical response with slightly higher levels predicted by the numerical simulations. It can be seen that the normalized rms pressure levels are almost constant in the spanwise direction, as highlighted by the isopressure contour maps plotted in Fig. 25 (left).

The PWL spectrum in the outlet duct is then calculated by coupling the CAA output data (vane-surface pressure) to the code FanNoise. In Fig. 26, our CAA result (black) is compared to Atassi and Vinogradov's solution (light) digitized from [20] and also to the Amiet-based prediction (dashed). Although the turbulent-inflow conditions are set constant, the Amiet-based calculation is performed by splitting the duct into several radial strips (10 in the present case) to account for mean-flow and stagger-angle variations in the spanwise direction, and the noncompactness of the noise sources along the

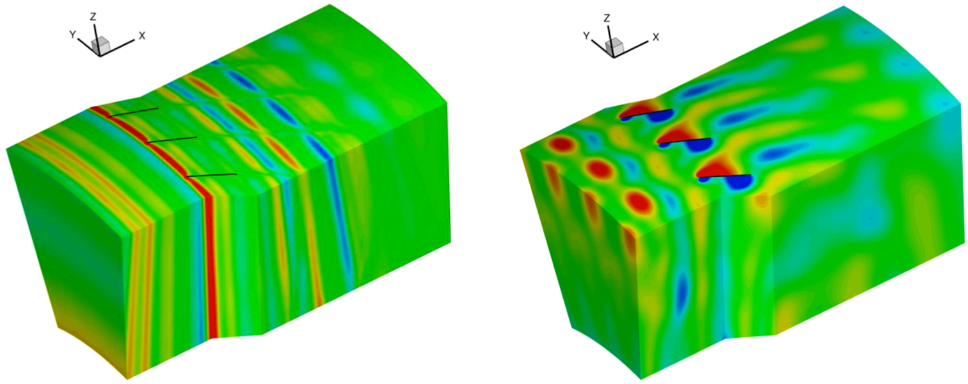

Fig. 24 Snapshots of azimuthal-velocity disturbances (±2 m/s, left) and pressure disturbances (±100 Pa, right) duplicated over three angular sectors.

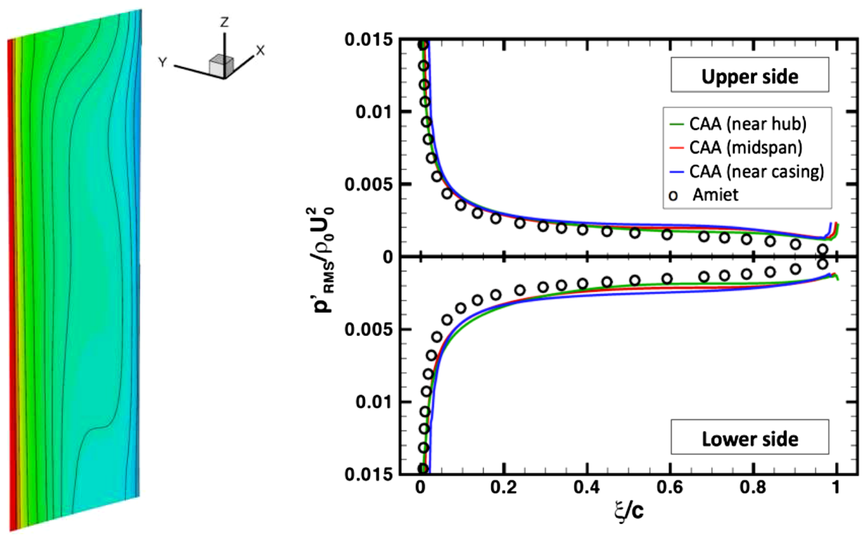

Fig. 25 CAA surface rms pressure (Pa) over the lower vane side (left) and chordwise normalized rms pressure profiles at three spanwise stations compared to the Amiet-based solution (right).

span. A very good agreement can be observed between the Atassi and Amiet-based predictions, which tends to show that the cascade effects are negligible for this configuration. On the other hand, the present CAA solution shows significant differences, with lower PWL and particularly a steep attenuation slope beyond 1500 Hz. This leads to an underprediction of −8 dB/Hz around 3000 Hz. Such differences with the Amiet-based result are surprising regarding the low discrepancies observed on the rms wall-pressure distributions (in Fig. 25, right).

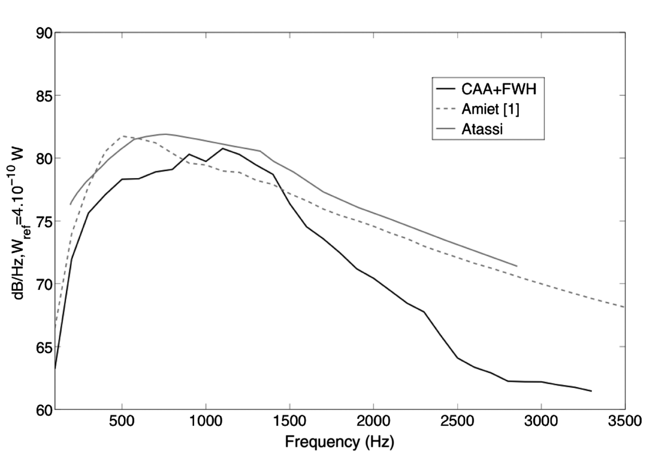

Fig. 26 PWL spectra (dB/Hz) provided by CAA + FWH and compared to Amiet-based and Atassi and Vinogradov [20] predictions.

To better understand the reasons for this mismatch, wall-pressure spectra have been analyzed. The typical results at two chordwise positions are presented in Fig. 27, comparing the numerical pressure PSD with Amiet's [1] theory, and in Fig. 28, showing the computed phase spectra. Near the leading edge, the shape and level of the computed spectra are found to be rather close to the Amiet-based predictions (in dotted lines), but important oscillations seem to appear at 10% chord. Nevertheless, the mean value of the oscillating level vs frequency, for each spanwise position, is relatively close to Amiet's [1] reference solution. An explanation for the discrepancies shown in Fig. 26 can be inferred from Fig. 28, in which significant phase variations between radial stations at 10% chord (Fig. 28, right) can be seen in the frequency range (2000–3300 Hz). Destructive interference effects could arise from these phase shifts along the span, when integrating the wall-pressure fluctuations in the FWH solver (whereas no phase shift is expected in Amiet's [1] approach with parallel gusts). As mentioned before, the parallel-gust restriction in the CAA might not be suited to realistic configurations with mean swirling flows.

To check this point, an FWH calculation has been run again by discarding the phase information along the span. (Source correlation is only considered in the chordwise direction.) The numerical prediction obtained by this way is plotted in Fig. 29 and compared to the previous solutions, showing an increase of the PWL up to 4 dB/Hz, and leading to a better agreement with Atassi and Vinogradov [20] results. This tends to confirm our interpretation and provides some limits of our present numerical method when discarding the oblique gusts for this second turbulence–cascade application case.

As done in Sec. IV.A, to check the accuracy of our numerical simulations and to confirm the aforementioned suggestions,

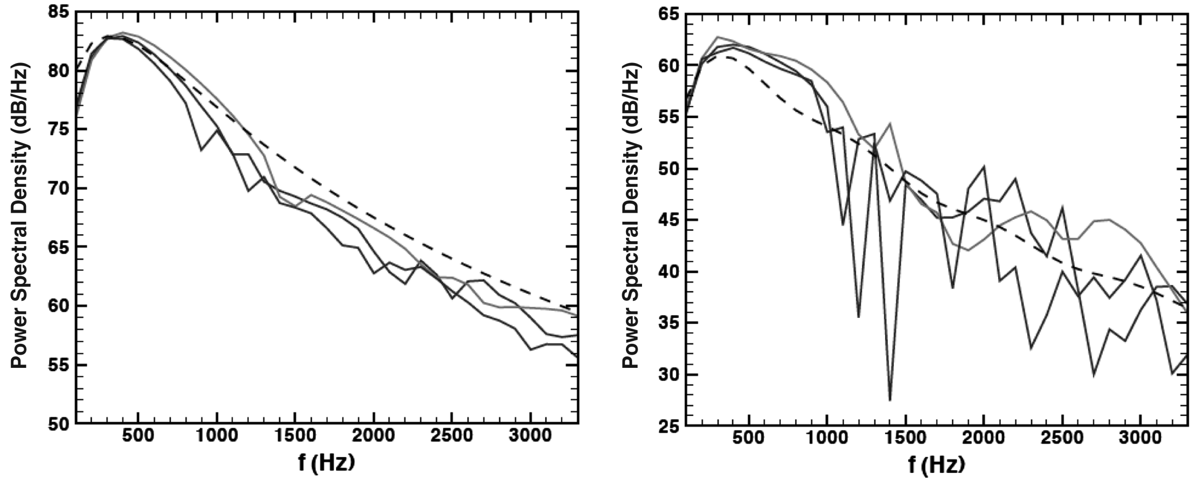

Fig. 27 CAA wall-pressure PSD (dB/Hz) on vane-pressure side (hub/light, midspan/medium, casing/dark) compared to Amiet-based solution (dotted line) at $\xi/c \approx 0$ (left) and $\xi/c = 0.1c$ (right).

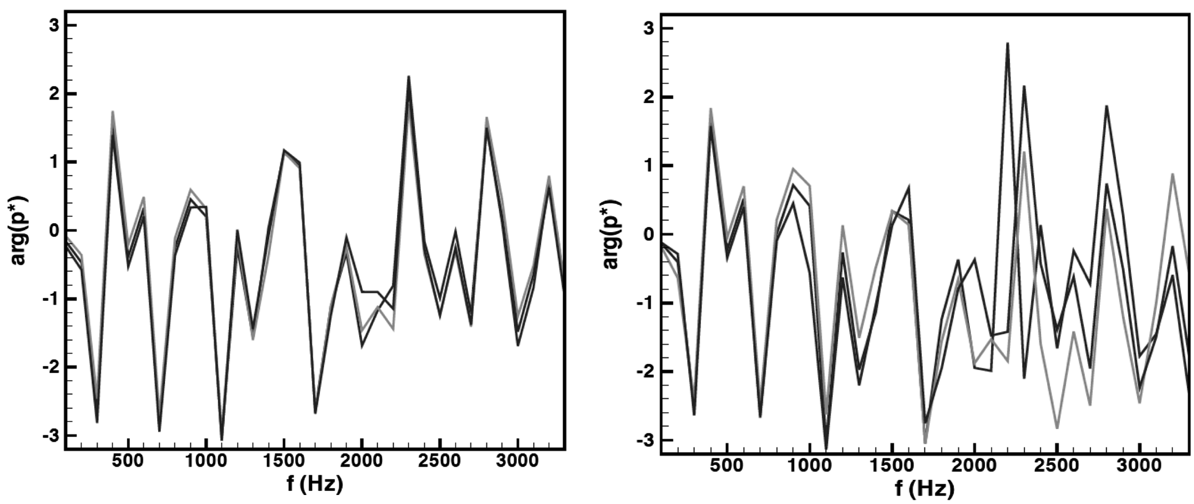

Fig. 28 CAA wall-pressure PSD phase (radians) on vane-pressure side (hub/light, midspan/medium, casing/dark) at $\xi/c \approx 0$ (left) and $\xi/c = 0.1c$ (right).

extended computations have been performed using the complete (k_x, k_r) turbulence spectrum in Eq. (8) and applying a double sum over the axial and radial wave numbers, as written in Eq. (1). The same CAA grid with identical computation parameters has been used. Moreover, to better estimate the PWL deviations related to statistical errors, three different sets of random phases have been used when generating the synthetic turbulence, leading to three independent runs and simulation results. Referring to the Shannon criterium, up to 21 radial modes [$M = 10$ in Eq. (1)] can be generated here, and convergence is achieved after two periods requiring about 10 h over 64 processors (comparable to the previous case).

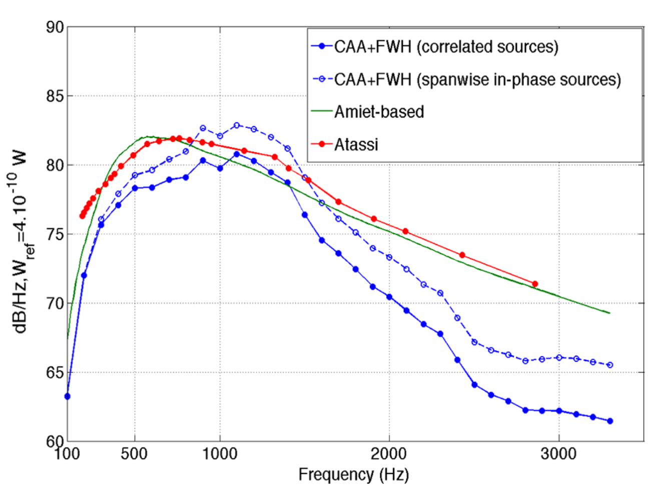

Fig. 29 PWL spectra (dB/Hz) provided by CAA + FWH compared to Amiet-based and Atassi and Vinogradov [20] solutions.

First of all, the computation results have been focused on wall-pressure analyses over the vanes. Typical solutions near the leading edge are presented in Fig. 30, in terms of pressure PSD (Fig. 30a) with associated phase spectra (Fig. 30b), for three radial positions (10%, 50%, and 90% span, as in Figs. 27 and 28). As expected, the pressure PSD shapes are much more oscillating (compared to those in Fig. 27, left) with higher levels too. Contrary to Fig. 28 (left), the phase spectra exhibit strong variations along the span due to the presence of the oblique gusts that should give rise to more relevant decorrelation effects. The PWL spectra in the outlet duct provided by the coupling with FanNoise code for the three different random-phase sets (three different CAA runs) are compared in Fig. 31. Despite the oscillations, the spectra display quite similar shapes so that a smoothing issued from a quadratic average of the levels would converge to very close solutions. To finish, the outlet duct PWL spectrum provided by the CAA using the complete spectrum (k_x, k_r) turbulence-spectrum model (and phase set 3) is compared to the one previously obtained [using (k_x, 0)] and to Atassi and Vinogradov [20] solution in Fig. 32. The numerical prediction is found to be clearly improved, showing a much better agreement with Atassi's spectrum, with a better assessment of the attenuation slope, despite slightly overpredicted

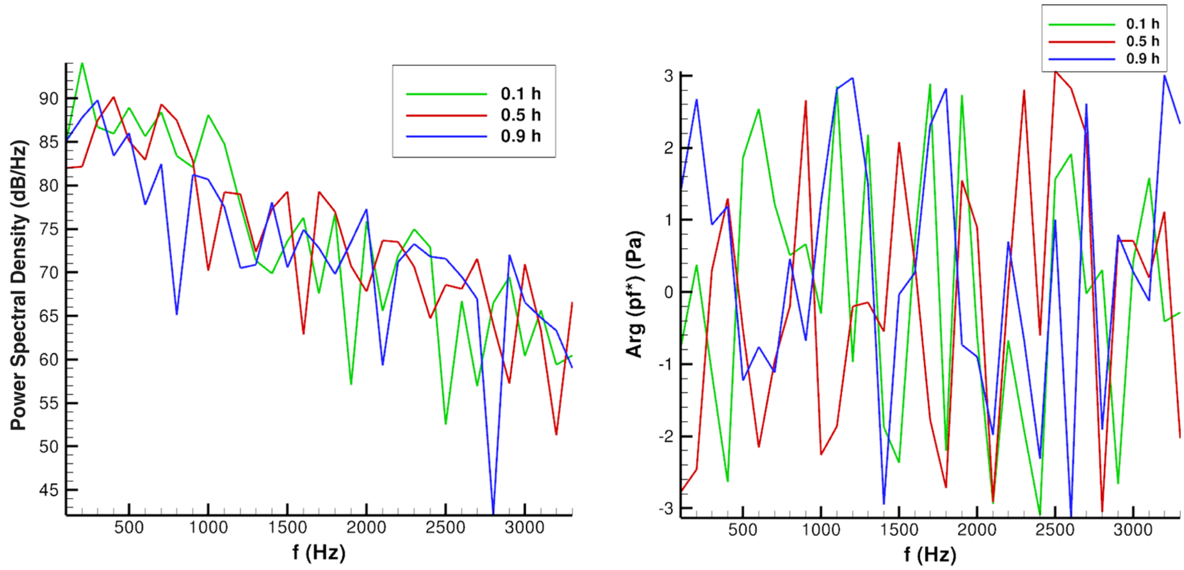

a) Pressure PSD (dB/Hz)

b) Phase spectra (rad)

Fig. 30 CAA predictions using complete synthetic turbulence with radial wave numbers: a) wall-pressure PSD and b) phase spectra (in radians), at three spanwise positions.

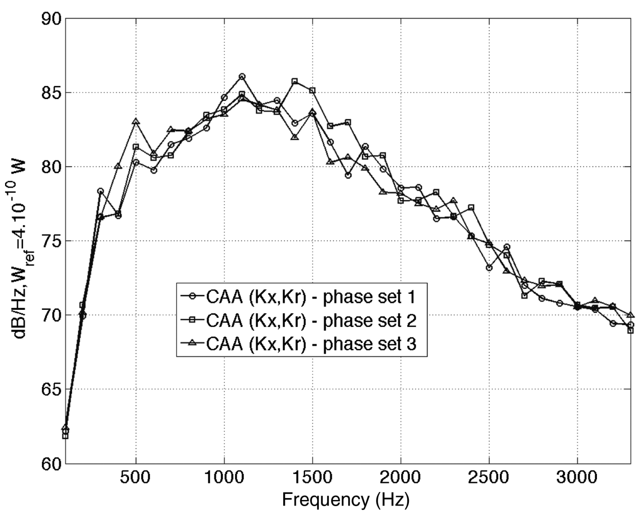

Fig. 31 Outlet duct PWL spectra (dB/Hz) issued from CAA with (k_x, k_r) turbulence spectrum using different sets of random phases.

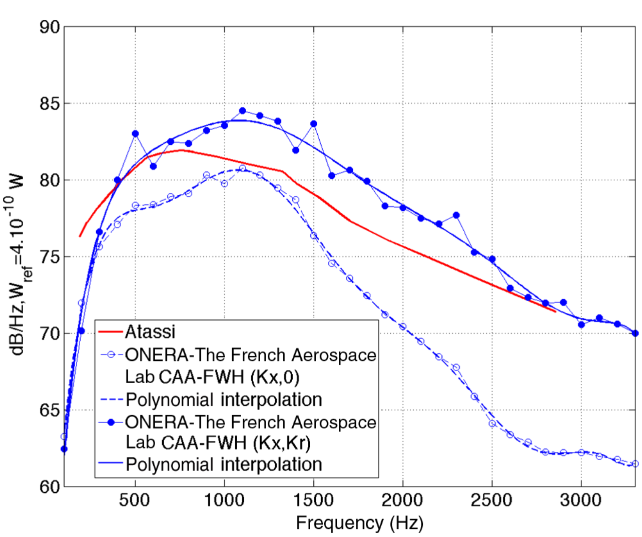

Fig. 32 Outlet duct PWL spectra (dB/Hz) provided by CAA + FWH using $(k_x, 0)$ and (k_x, k_r) turbulence spectra, and compared to Atassi and Vinogradov [20] solution.

levels (no more than 3 dB). This is a very promising result that tends to validate the present method, and suggests to use the complete two-wave-number turbulence model for rotor–stator applications.

V. Conclusions

A hybrid methodology based on a 3-D CAA/Euler solver coupled to a stochastic model aiming at generating a synthetic turbulent inflow has been presented in this paper. Suited Tam's BCs [14] have been implemented into the code to ensure a nonreflecting injection of velocity disturbances, and have been associated to a sponge zone at the exit for outgoing acoustic/hydrodynamic modes. Simulations have been conducted on annular flat-plate cascade configurations with prescribed inflow disturbances impinging the flat-plate vanes. Both uniform and swirling mean-flow cases have been investigated, and the numerical predictions have been successfully compared to semi-analytical solutions and to experimental data (when available). Sound-propagation simulations in the duct are practically achieved by chaining the CAA code to an FWH solver for broadband-noise calculations.

The present method has been first validated against a harmonic CAA benchmark proposed by NASA, showing an excellent agreement. The use of a two-wave-number (streamwise and spanwise) turbulence spectrum resulting from an integration of the three-wave-number spectrum over the azimuthal direction has been suggested to limit the computation domain to a single vane channel. Furthermore, by analogy with Amiet's [1] theory, synthetic turbulence can be restricted to parallel gusts (setting the spanwise wave number equal to zero). This allows the considerable reduction of the CPU costs. The predictions here, applied to two tested cascades immersed in a turbulence convected by a purely axial mean flow, are found to be close to the semi-analytical solutions based on the lifting-surface method and to the measurements. It has been verified that the addition of oblique gusts (spanwise wave numbers) leads to almost the same PWL spectra when the mean flow is purely axial. The first application to a more realistic swirling mean-flow case (involving a radial evolution of the convection flow and stagger angle) has been investigated then, showing that the spanwise wave-number contribution has to be included into the CAA simulations to capture realistic decorrelation effects along the span. By this way, the present numerical predictions were found to be in a rather good agreement with Atassi and Vinogradov [20] reference solution.

The next step will be to apply the method to a turbofan stage model configuration, like the Source Diagnostic Test from NASA Glenn Research Center, recently benchmarked using semi-analytical [19] and numerical [7,27] methods, and to adjust the turbulent-inflow characteristics from hot-wire measurements or from a Reynolds-averaged Navier–Stokes computation data.

Appendix: Amiet-Based Prediction of Rotor/Stator-Interaction Broadband Noise

Hereafter, a short description of the formulation developed in [24] is presented. The model is based on the prediction of the surface-pressure spectral density over the stator (cascade) vane using an aeroacoustic transfer function based on Amiet's theory [1] (isolated-airfoil response assimilated to a flat plate) and coupled to the FWH formulation (loading-noise term) extended by Goldstein [22] using a Green's function valid for an annular duct and a uniform mean flow. We use a bidimensional form of the Amiet-based response by only considering the parallel gusts. This hypothesis is justified for large aspect ratio ($L/c \geq 3$) and allows very fast predictions, because no integration over the radial wave numbers is necessary. Hence, we can easily apply a strip theory that consists in splitting the incoming turbulence characteristics in several slices along the span and performing an incoherent sum of each slice contribution. Sources are distributed over each strip center, so that the formulation is partially noncompact.

The flat-plate attached coordinate system (ξ, η, r) in the x-axis duct frame is sketched in Fig. A1.

The classical expression of the PWL spectrum, $S_{ww}(f)$, writes

$$S_{ww}^{\pm}(f) = \sum_{m=-m_{\max}}^{m_{\max}} \sum_{n=1}^{n_{\max}} \frac{\Gamma_{mn} r_t^2}{\rho_0 c_0} \frac{K(\beta^2 k_{mn}^{\pm} + M_x K)}{(K - M_x k_{mn}^{\pm})^2} E[|A_{mn}^{\pm}(f)|^2] \tag{A1}$$

The sign $\pm$ denotes downstream $(+)$ and upstream $(-)$ propagation, K is the total acoustic wave number, $k_{mn}^{\pm}$ is the axial wave number of the mode (m, n), $\beta^2 = 1 - M_x^2$ with M_x is the axial Mach number in the duct, and Γ_{mn} is the normalization factor (over the duct cross section) of the orthogonal eigenfunctions. $E[|A_{mn}^{\pm}(f)|^2]$ is the ensemble average of the duct-mode amplitude A_{mn}. In the present model, this last quantity is given for one strip at the spanwise station $r = r_s$, by

$$E[|A_{mn}^{\pm}(\omega)|^2] = \frac{4\pi d(\pi\rho_0 b)^2 U_c}{|\Delta_{mn}|^2 \Gamma_{mn}^2} \left[\left(k_{mn} \sin\chi - \frac{m \cos\chi}{r_s} \right) C_{mn}(r_s) \right]^2 \times \phi_{\eta\eta}(k_c, 0) |\ell_{mn}^{\pm}(r_s, k_c, 0)|^2 \tag{A2}$$

In the last equation, d is half the size of the considered strip, b is the half-chord, and χ is the stagger angle. The incoming turbulence is supposed to be homogeneous, uniform azimuthally, and frozen with a convection velocity U_c and a convection wave number, $k_c = \omega/U_c$. The fluctuations of the upwash-velocity component (normal to the chord) are described by the upwash-velocity spectrum $\phi_{\eta\eta}$. Δ_{mn} is the cutoff ratio of the mode (m, n), and C_{mn} is the radial eigenfunction.

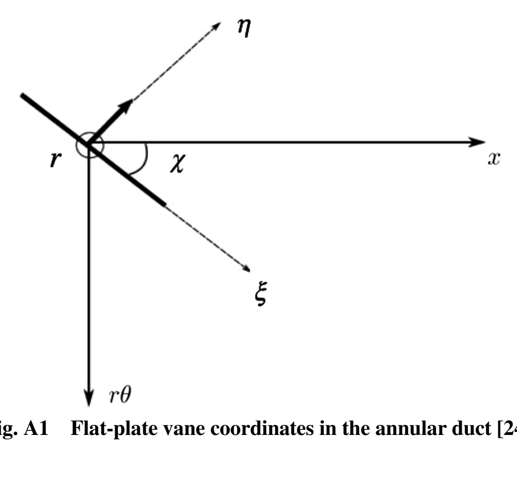

Fig. A1 Flat-plate vane coordinates in the annular duct [24].

(Suited normalized functions are adopted, so that $\Gamma_{mn} = 2\pi$.) Finally, ℓ_{mn} is an aeroacoustic modal transfer function, related to Amiet's [1] response function g in Eq. (A3)

$$\ell_{mn}^{\pm}(r_s, k_c, k_r) = \frac{1}{b} \int_{-b}^{b} g(\xi, k_c, k_r) e^{i\varphi_{mn}^{\pm}(r_s)\xi} \,\mathrm{d}\xi \tag{A3}$$

The phase term φ_{mn} is related to the Green's function at source position (s index on axial and angular cylindrical coordinates) and defined by

$$\varphi_{mn}^{\pm}(r_s)\xi = m\theta_s + k_{mn}^{\pm} x_s \tag{A4}$$

Following Amiet's methodology [1], it is possible to split ℓ_{mn} in two parts: a main term, ℓ_{mn}^1, corresponding to the contribution of the leading edge, and a correction term, ℓ_{mn}^2, induces by the trailing edge. For supercritical gusts ($k_r \leq k_c M_c/\beta$):

$$\ell_{mn}^1(r_s, k_c, k_r) = \frac{1}{\pi} \sqrt{\frac{2}{(k_c b + \beta^2 \kappa)\theta_1}} e^{i\theta_2} F^*[2\theta_1] \tag{A5}$$

$$\ell_{mn}^2(r_s, k_c, k_r) = \frac{e^{i\theta_2}}{\pi\theta_1 \sqrt{2\pi(k_c b + \beta^2\kappa)}} \times \left[(1-i) \left(F^*[4\kappa] - \sqrt{\frac{2\kappa}{2\kappa - \theta_1}} e^{-i\theta_1} \{F^*[2(2\kappa - \theta_1)]\} \right) + i(1 - e^{-i2\theta_1}) \right] \tag{A6}$$

in which $\kappa^2 = \mu^2 - (k_r^2 b/\beta^2)$, $\mu = M_c k_c b/\beta^2$, $\theta_1 = \kappa - M_c\mu - b\varphi_{mn}(r_s)$, $\theta_2 = -b\varphi_{mn}(r_s) - \pi/4$, and F^* is the conjugate of the complex Fresnel integral. The expressions for subcritical gust are available in [24], but are not practically required because spanwise wave numbers k_r are discarded.

Acknowledgments

This work was partly conducted in the framework of the LabEx Centre Lyonnais d'Acoustique of the Université de Lyon, operated by the French National Research Agency. The authors would like to thank Julissa Grondin (Master's student at the École Centrale de Lyon) for the updated computational aeroacoustics simulations with oblique gusts realized during her internship at ONERA.

References

[1] Amiet, R. K., "Acoustic Radiation from an Airfoil in Turbulent Stream," *Journal of Sound and Vibration*, Vol. 41, No. 4, 1975, pp. 407–420. doi:10.1016/S0022-460X(75)80105-2

[2] Hanson, D., "Broadband Noise of Fans: With Unsteady Coupling Theory to Account for Rotor and Stator Reflection/Transmission Effects," NASA CR-211136, 2001.

[3] Riou, J., Léwy, S., and Heib, S., "Large Eddy Simulation for Predicting Rotor–Stator Broadband Interaction Fan Noise," *Inter-Noise2007 Conference*, Turkish Acoustical Soc., Turkey, 2007.

[4] Greschner, B., and Thiele, F., "Wall Modeled LES Simulation of Rotor–Stator-Cascade Broadband Noise," *17th AIAA/CEAS Aeroacoustics Conference*, AIAA Paper 2011-2873, June 2011.

[5] Laborderie, J., Moreau, S., and Berry, A., "Compressor Stage Broadband Noise Prediction Using a Large-Eddy Simulation and Comparisons with a Cascade Response Model," AIAA Paper 2013-2042, May 2013.

[6] Li, Q., Peake, N., and Savill, M., "Large Eddy Simulations for Fan-OGV Broadband Noise Prediction," AIAA Paper 2008-2843, May 2008.

[7] Mann, A., Perot, F., Kim, M.-S., Casalino, D., and Fares, E., "Advanced Noise Control Fan Direct Aeroacoustics Predictions Using a Lattice-

Boltzmann Method," *18th AIAA/CEAS Aeroacoustics Conference*, AIAA Paper 2012-2287, June 2012.

[8] Clair, V., Polacsek, C., Le Garrec, T., Reboul, G., Gruber, M., and Joseph, P., "Experimental and Numerical Investigation of Turbulence–Airfoil Noise Reduction Using Wavy Edges," *AIAA Journal*, Vol. 51, No. 11, 2013, pp. 2695–2713. doi:10.2514/1.J052394

[9] Dieste, M., and Gabard, G., "Random Particle Methods Applied to Broadband Fan Interaction Noise," *Journal of Computational Physics*, Vol. 231, No. 24, 2012, pp. 8133–8151. doi:10.1016/j.jcp.2012.07.044

[10] Wohlbrandt, A. M., Guerin, S., and Ewert, R., "Simultaneous Computation of Surface and Volume Sources for Fan Broadband Noise with the Random-Particle-Mesh Method," *19th AIAA/CEAS Conference*, AIAA Paper 2013-2119, May 2013.

[11] Clair, V., Polacsek, C., Le Garrec, T., and Jacob, M., "Numerical Predictions of Turbulence–Cascade Interaction Noise Using CAA with a Stochastic Model," *20th AIAA/CEAS Aeroacoustics Conference*, AIAA Paper 2014-2453, June 2014.

[12] Redonnet, S., Manoha, E., and Sagaut, P., "Numerical Simulations of Propagation of Small Perturbations Interacting with Flows and Solid Bodies," *7th AIAA/CEAS Aeroacoustics Conference*, Paper 2001-0222, May 2001.

[13] Redonnet, S., Desquesnes, G., Manoha, E., and Parzini, C., "Numerical Study of Acoustic Installation Effects with a Computational Aeroacoustics Method," *AIAA Journal*, Vol. 48, No. 5, 2010, pp. 929–937. doi:10.2514/1.42153

[14] Tam, C. K. W., "Advances in Numerical Boundary Conditions for Computational Aeroacoustics," *Journal of Computational Acoustics*, Vol. 6, No. 4, 1998, pp. 377–402. doi:10.1142/S0218396X98000259

[15] Namba, M., and Schulten, J., "Third Computational Aeroacoustics (CAA) Workshop on Benchmark Problems: Category 4—Fan Stator with Harmonic Excitation by Rotor Wake," NASA TM-2000-209790, 2000, pp. 73–85.

[16] Namba, M., "Three-Dimensional Analysis of Blade Force and Sound Generation for an Annular Cascade in Distorted Flows," *Journal of Sound and Vibration*, Vol. 50, No. 4, 1977, pp. 479–508. doi:10.1016/0022-460X(77)90498-9

[17] Schulten, B., "Sound Generated by Rotor Wakes Interacting with a Leaned Vane Stator," *AIAA Journal*, Vol. 20, No. 10, 1982, pp. 1352–1358. doi:10.2514/3.51195

[18] Posson, H., and Roger, M., "Experimental Validation of a Cascade Response Function for Fan Broadband Noise Predictions," *AIAA Journal*, Vol. 49, No. 9, 2011, pp. 1907–1918. doi:10.2514/1.J050728

[19] Envia, E., and Coupland, J., "AA-39 Panel Session: Fan Broadband Noise Prediction," *20th AIAA/CEAS Aeroacoustics Conference*, 2014, www.oai.org/aeroacoustics/FBNWorkshop/.

[20] Atassi, H., and Vinogradov, I., "Modeling Broadband Fan Noise and Comparison with Experiments," *13th AIAA/CEAS Aeroacoustics Conference*, AIAA Paper 2007-3691, May 2007.

[21] Atassi, H., Ali, A., Atassi, O., and Vinogradov, I., "Scattering of Incident Disturbances by an Annular Cascade in a Swirling Flow," *Journal of Fluid Mechanics*, Vol. 499, Jan. 2004, pp. 111–138. doi:10.1017/S0022112003007031

[22] Goldstein, M.-E., *Aeroacoustics*, McGraw–Hill, New York, 1976, pp. 63–66.

[23] Reboul, G., Polacsek, C., Lewy, S., and Heib, S., "Ducted-Fan Broadband Noise Simulations Using Unsteady or Averaged Data," *Inter-Noise 2008 Conference*, Inst. of Acoustics/Chinese Academy of Science, China, 2008.

[24] Reboul, G., "Modélisation du bruit à large bande de soufflante de turboréacteur," Ph.D. Thesis, École Centrale de Lyon, France, 2010.

[25] Zhang, W., Wang, X., and Sun, X., "A Broadband Noise Model for Turbulence/Annular Cascade Interaction," *19th AIAA/CEAS Aeroacoustics Conference*, AIAA Paper 2013-2243, May 2013.

[26] Bogey, C., and Bailly, C., "Three-Dimensional Non-Reflective Boundary Conditions for Acoustic Simulations: Far-Field Formulation and Validation Test Cases," *Acta Acustica*, Vol. 88, No. 4, March 2002, pp. 463–471.

[27] Sescu, A., "Towards Computational Aeroacoustics Prediction of Realistic Turbofan Noise Using Synthetic Turbulence Modeling," Ph.D. Thesis, Univ. of Toledo, Spain, 2011.

[28] Kraichnan, R., "Diffusion by a Random Velocity Field," *Physics of Fluids*, Vol. 13, No. 1, 1970, pp. 22–31. doi:10.1063/1.1692799

[29] Salem Said, A.-H., "Large Eddy Simulation of Shear-Free Interaction of Homogeneous Turbulence with a Flat-Plate Cascade," Ph.D. Thesis, Virginia Polytechnic Inst. and State Univ., Virginia, 2007.

[30] Ewert, R., "Broadband Slat Noise Prediction Based on CAA and Stochastic Sound Sources from a Random Particle Mesh (RPM) Method," *Computers and Fluids Journal*, Vol. 37, No. 4, 2008, pp. 369–387. doi:10.1016/j.compfluid.2007.02.003

[31] Casper, J., and Farassat, F., "Broadband Noise Predictions Based on a New Aeroacoustic Formulation," *40th Aerospace Sciences Meeting and Exhibit*, AIAA Paper 2002-0802, Jan. 2002.

[32] Hixon, R., Sescu, A., and Sawyer, S., "Vortical Gust Boundary Condition for Realistic Rotor Wake/Stator Interaction Noise Prediction Using Computational Aeroacoustics," *Journal of Sound and Vibration*, Vol. 330, No. 16, 2011, pp. 3801–3817. doi:10.1016/j.jsv.2011.03.011

[33] Tyler, M., and Sofrin, T. G., "Axial Flow Compressor Noise Studies," *SAE Transactions*, Vol. 70, Jan. 1962, pp. 309–332.

[34] Golubev, V., and Atassi, H., "Unsteady Swirling Flows in Annular Cascades, Part 1: Evolution of Incident Disturbances," *AIAA Journal*, Vol. 38, No. 7, 2000, pp. 1148–1149.

C. Bailly
Associate Editor